

Dynamic Weakening and the Depth Dependence of Earthquake Faulting

Nicolas Brantut¹ and John D. Platt²

ABSTRACT

Earthquake propagation is controlled by both the applied stresses and the dynamic frictional strength of fault rocks. Dynamic friction of rocks is characterized by strong weakening driven by shear heating and power dissipation. Here, we investigate the efficiency of two major weakening mechanisms, flash heating and thermal pressurization, as a function of depth across a range of representative geological settings. We first determine the relevant characteristic parameters for each mechanism. Flash heating is activated above a critical weakening velocity and controlled by two critical weakening times; thermal pressurization is controlled by a critical weakening strain at small slip and a critical weakening slip at large slip. We quantify how these parameters vary with pressure and temperature according to available published data, computing their values as a function of depth for a range of geological settings. We find that thermal pressurization is most efficient at shallow depths, with a peak efficiency at mid-crustal depths, while flash heating is most efficient in deeper parts of the faults. If driven by flash heating, earthquake ruptures appear to be able to propagate through the brittle-plastic transition. The arrest of ruptures at further depth is likely due to the decrease in the background driving stress.

9.1. INTRODUCTION

The Earth's seismicity is largely confined to the upper crust, typically above the 600°C isotherm [McKenzie *et al.*, 2005], where rocks accommodate deformation by brittle failure. The maximum strength of the seismogenic crust is generally assumed to be the frictional resistance to sliding on an optimally oriented fault plane, which is well approximated by a frictional rupture envelope with a friction coefficient between 0.6 and 0.8 [e.g., Brace and Kohlstedt, 1980; Kohlstedt *et al.*, 1995]. However, this strength estimate is *local* and *static*: it is a measure of whether a faulted rock can slide or not. As such, it bears

no information about the *stability* of fault slip, which determines whether frictional deformation is steady and stable or whether earthquakes (i.e., unstable, fast, slip events) dominate the dynamics of faulting.

Determining when earthquake nucleation occurs requires additional knowledge about the details of the frictional constitutive law on the fault. In the framework of rate and state constitutive friction laws, a number of authors [e.g., Dieterich, 1978; Ruina, 1983] have demonstrated that the key parameter controlling the nucleation of earthquakes is the rate dependency of friction: steady-state velocity-strengthening faults slide stably while steady-state velocity-weakening faults are prone to dynamic instabilities. These theoretical considerations are supported by experimental and geological observations that show the depth distribution of seismicity in the crust and in subduction zones closely matches the depth dependence of the velocity-strengthening/weakening parameter of fault rocks, with shallow seismicity markedly decaying

¹Rock and Ice Physics Laboratory and Seismological Laboratory, Department of Earth Sciences, University College London, London, UK

²Department of Terrestrial Magnetism, Carnegie Institution for Science, Washington, DC, USA

above the depth of the transition from velocity-weakening to velocity-strengthening friction [e.g., *Marone and Scholz*, 1988; *Scholz*, 1998]. Stability analyses have shown that the earthquake nucleation size is much smaller (typically a few meters to tens of meters) than typical fault dimensions [e.g., *Rice and Ruina*, 1983; *Rice et al.*, 2001; *Rubin and Ampuero*, 2005; *Ampuero and Rubin*, 2008]. This raises the key following question: If an earthquake nucleates on a small portion of a fault, what controls its propagation and depth extent?

In contrast with local considerations of static strength, the problem of earthquake propagation is essentially a *non local* problem. Slip redistributes stress along the fault, with large stresses concentrated near the rupture tip, allowing slip to occur dynamically in regions where the initial background stress prior to the earthquake is significantly lower than the static brittle strength [e.g., *Rice*, 1996; *Lapusta and Rice*, 2003; *Rice*, 2006; *Noda et al.*, 2009]. The minimum background stress level above which earthquakes can propagate is controlled by how the fault dynamically weakens with increasing slip and slip rate. Therefore, the extent of seismic ruptures is controlled by a balance between the initial background stress distribution, which represents the stored elastic energy density, and the dynamic strength of the fault, which determines when and where energy is dissipated on the fault plane.

In the past decade, a number of experimental and theoretical studies have shown that fault rocks tend to weaken dramatically at high slip rates (typically above 0.1 m/s) [e.g., *Di Toro et al.*, 2011]. The weakening mechanisms vary between rock types and experimental conditions, but all are driven by the high dissipation rates associated with the onset of rapid slip. For dry rocks the dominant dynamic weakening mechanism in the earliest stages of slip is flash heating at asperity contacts [e.g., *Rice*, 1999, 2006; *Beeler et al.*, 2008; *Goldsby and Tullis*, 2011]. In this process, the macroscopic friction coefficient decreases at high slip rates because the local frictional heating at highly stressed asperity contacts is sufficient to melt or thermally decompose them. The slip displacement required to activate flash heating is comparable to the size of asperities, typically a few tens of micrometers, so flash heating commences as soon as dynamic rupture starts, provided that the slip rate exceeds a critical value. As we will show in section 9.2, even at moderate slip rates the increase in bulk temperature due to frictional heating tends to facilitate the activation of flash heating, so that this mechanism is likely to play a major role throughout dynamic ruptures.

Thermal pressurization is another dynamic weakening mechanism driven by thermal expansion of in-situ pore fluid [e.g., *Lachenbruch*, 1980; *Mase and Smith*, 1985, 1987; *Rice*, 2006], which leads to a decrease in effective stress and thus fault strength. Most estimates show that

thermal pressurization is expected to become significant for slips larger than a centimeter and potentially leads to a total loss of strength [e.g., *Noda and Shimamoto*, 2005; *Wibberley and Shimamoto*, 2005; *Rice*, 2006; *Rempel and Rice*, 2006]. Other weakening mechanisms may provide significant dynamic weakening at larger slips, including melting [e.g., *Hirose and Shimamoto*, 2005; *Di Toro et al.*, 2005], gel formation [*Goldsby and Tullis*, 2002; *Di Toro et al.*, 2004], or thermal decomposition [e.g., *Han et al.*, 2007; *Hirose and Bystricky*, 2007; *Brantut et al.*, 2008].

In order to understand what controls the maximum depth of earthquake propagation, we constrain the efficiency of flash heating and thermal pressurization as a function of depth in the crust. The term *efficiency* used here and throughout this chapter is defined as the rapidity with which the local fault strength decreases at the onset of slip. With increasing depth, changes in the ambient temperature, effective pressure, and physical properties of fault rocks (e.g., permeability, porosity) and pore fluid (thermal expansivity, compressibility) alter the efficiency of dynamic weakening significantly. In section 9.2, we review and further develop the physical models and key parameters governing weakening by flash heating and thermal pressurization. In section 9.3 we present and discuss the parameter values used as inputs for the two weakening models, as well as our selection of geotherms and rock types for three seismogenic environments: a continental strike-slip fault, an oceanic transform fault, and a subduction megathrust. The resulting profiles of the key weakening parameters, described in section 9.4, indicate that flash heating becomes increasingly efficient with depth, while thermal pressurization is most efficient at mid-crustal depths. Our results show that despite the high efficiency of flash heating at great depth, the relatively low background stress allowed by long-term creep mechanisms tends inevitably to stop earthquake propagation through the lower crust.

9.2. THERMALLY ACTIVATED WEAKENING MECHANISMS

In this section we summarize the theoretical background used to quantify the efficiency of thermal pressurization and flash heating. We study each mechanism in isolation, aiming to find a limited set of characteristic parameters that controls the rapidity and efficiency of weakening. In what follows, we emphasize the natural variables characterizing each model (e.g., slip, time, or strain) and the sensitivity to the exact slip rate history of the fault. Because we eventually aim to characterize the potency for rupture propagation, one key parameter to compute for each mechanism, context, and depth is the shear fracture energy G . Fracture energy is only well defined for a purely slip-dependent friction law with a constant residual

strength beyond a threshold slip [Palmer and Rice, 1973], a situation unlikely to occur during seismic slip. To avoid this issue, we use here the generalization given by Rice [2006], who defines G for an event with slip δ as

$$G(\delta) = \int_0^\delta [\tau(\delta') - \tau(\delta)] d\delta', \quad (9.1)$$

where τ is the shear stress on the fault and δ is slip. Equation (9.1) is only valid for a monotonically decreasing shear strength $\tau(\delta)$, which will be the case throughout this paper. Complex rupture histories, including self-healing ruptures, would typically involve restrengthening near the rupture's tail, in which case a more general formula for G ought to be used [see, for instance, Garagash, 2012].

9.2.1. Flash Heating

Flash heating, adapted for rocks by Rice [1999, 2006] from a similar concept established in metal friction [Archard, 1958/1959], is based on the idea that the *local* temperature rise of a highly stressed frictional asperity far exceeds the average bulk temperature rise. The high temperatures at these microscale asperities during rapid slip trigger weakening mechanisms such as melting or thermal decomposition at the contact scale that lead to significant drops in the macroscopic friction coefficient. The analysis of flash heating presented in this section summarizes previous theoretical results obtained by Rice [1999], Rice [2006], Rempel [2006], Beeler *et al.* [2008], Proctor *et al.* [2014] and Platt *et al.* [2014a], and we refer the reader to these studies for further details of the analysis.

To begin, we use the slip rate V and a typical asperity contact size D to estimate the contact lifetime

$$t_{\text{con}} = \frac{D}{V}. \quad (9.2)$$

For typical seismic slip rates of the order of 1 ms^{-1} and contact sizes of a few tens of microns, t_{con} is just a few tens of microseconds, allowing us to assume that the slip rate and bulk fault temperature T do not change during the lifetime of a single contact. Assuming that all sliding occurs on a plane, we use a Green's function to solve for the temperature evolution of the contact,

$$T_{\text{con}} = T + \frac{\tau_c V}{\rho c} \sqrt{\frac{1}{\pi \alpha_{\text{th}}}}, \quad (9.3)$$

where T is the fault bulk temperature, τ_c is the shear stress supported by the contact, t is the time since the contact came into existence, ρc is the effective heat capacity per unit reference volume, and α_{th} is the thermal

diffusivity. Next we assume that weakening occurs if the contact temperature exceeds a weakening temperature T_w , which corresponds to a threshold temperature for either melting or thermal breakdown of the contact. Equation (9.3) shows that the contact temperature reaching T_w is equivalent to the contact lifetime exceeding a critical weakening timescale

$$t_{\text{cw}} = \pi \alpha_{\text{th}} \left(\frac{\rho c (T_w - T)}{\tau_c V} \right)^2. \quad (9.4)$$

Thus, flash heating occurs if $t_{\text{con}} > t_{\text{cw}}$, which is equivalent to the slip rate exceeding a critical weakening slip rate

$$V_w(T) = \frac{\pi \alpha_{\text{th}}}{D} \left(\frac{\rho c (T_w - T)}{\tau_c V} \right)^2. \quad (9.5)$$

Next we predict the dependence of the macroscopic friction coefficient on slip rate when flash heating is active by calculating the time the contact spends in the weakened and unweakened states. We assume that in the unweakened state the macroscopic friction coefficient is f_0 and model weakening by lowering this value to a weakened friction coefficient f_w . As shown in Rice [2006] and Beeler *et al.* [2008], the macroscopic friction is equal to

$$f = f_0 \frac{t_{\text{cw}}}{t_{\text{con}}} + f_w \left(1 - \frac{t_{\text{cw}}}{t_{\text{con}}} \right), \quad (9.6)$$

which rearranges to give

$$f = (f_0 - f_w) \frac{V_w(T)}{V} + f_w. \quad (9.7)$$

The assumption that weakening can be modeled by instantaneously dropping the contact strength to a weakened value is crude, though Rempel and Weaver [2008] and Chen and Rempel [2014] developed a better model accounting for the thin melt layer that forms at a contact. However, Goldsby and Tullis [2011] found good agreement with equation (9.7) in experiments on a range of materials, suggesting that this formula provides a good first-order estimate of the weakening from flash heating.

In the previous steps we assumed that the contact scale slip rate is equal to the macroscopic slip rate. While this assumption is valid for sliding of bare surfaces, it is not a good approximation for distributed deformation in a gouge. Rempel [2006] and Beeler *et al.* [2008] modeled flash heating in a gouge by assuming that the total slip rate is shared between an array of contacts. For an array of contacts, weakening occurs when the *local* slip rate at each contact reaches the nominal weakening slip rate V_w ,

which implies that the effective weakening velocity for slip across gouge is, on average,

$$V_{w,\text{gouge}}(T) = V_w(T) \times N_c, \quad (9.8)$$

where N_c is the number of contacts mobilized across the gouge and is typically around 10 to 20 (see *Rice* [2006], section 1.1).

While flash heating is naturally expressed in terms of a critical weakening slip rate and previous experiments have mostly focused on the slip rate dependence, *Platt et al.* [2014a] recently argued that temperature effects dominate flash heating at seismogenic depths. The critical weakening slip rate decreases as the fault temperature rises, leading to potentially significant weakening, as demonstrated experimentally in *Proctor et al.* [2014]. To quantify the temperature weakening effects, we model the evolution of fault bulk temperature during seismic slip. Initially the thermal boundary layer adjacent to the deforming gouge is much smaller than the gouge thickness and therefore the early stages of slip occur under mostly adiabatic conditions. By contrast, for large slips (or a thin gouge layer) the thermal boundary layer becomes much wider than the shear zone width, and the behavior is expected to be well approximated by a model in which slip occurs on a mathematical plane. In the remainder of this section we develop these two end-member solutions and determine the associated characteristic weakening parameters.

To model flash heating under macroscopically adiabatic conditions, we follow the model of *Platt et al.* [2014a]. Conservation of energy leads to an equation for the bulk temperature T :

$$\frac{\partial T}{\partial t} = \frac{\tau V}{\rho c W}, \quad (9.9)$$

Where τ is the macroscopic shear strength of the gouge layer and W is the thickness of the deforming gouge. Setting the shear strength equal to the product of the ambient effective stress ($\sigma_n - p_0$) and the velocity-dependent friction coefficient, we obtain

$$\frac{\partial T}{\partial t} = \frac{f_0(\sigma_n - p_0)}{\rho c} \frac{\pi \alpha_{\text{th}}}{DW N_c} \left(\frac{\rho c (T_w - T)}{\tau_c} \right)^2, \quad (9.10)$$

where we have assumed that $f_w = 0$ and that the slip rate is greater than the initial value of V_w . Note that because the friction coefficient for flash heating is proportional to $1/V$, the rate of frictional heating, and thus the evolution of V_w is independent of slip rate. However, the friction coefficient is controlled by the ratio V_w/V so

the shear strength evolution of flash heating is sensitive to the exact slip rate history of the fault.

We solve equation (9.10) to find the bulk temperature evolution

$$T(t) = T_0 + (T_w - T_0) \frac{t}{t + t_w^A}, \quad (9.11)$$

which is controlled by the critical weakening timescale for adiabatic conditions

$$t_w^A = \frac{(W/N_c) D \tau_c^2}{f_0(\sigma_n - p_0) \pi \alpha_{\text{th}} \rho c (T_w - T_0)}. \quad (9.12)$$

Inserting equation (9.11) for the temperature evolution in the gouge into the constitutive relation (7) (with the critical velocity $V_{w,\text{gouge}}$), we observe that the shear stress evolution is controlled by the weakening time t_w^A . Using the shear stress evolution $\tau(t) = f(t) \times (\sigma_n - p_0)$, we find that the fracture energy for flash heating under adiabatic conditions is

$$G(t) = W \rho c (T_w - T_0) \frac{t}{t_w^A + t} \left(1 - \frac{t_w^A}{t_w^A + t} \right), \quad (9.13)$$

which tends to

$$G_{\text{FH}}^A = W \rho c (T_w - T_0) \quad (9.14)$$

for $t \gg t_w^A$. The fracture energy is simply the energy required to heat the gouge from the ambient temperature T_0 up to the weakening temperature T_w .

At large slips, where the shear zone width is much smaller than the thickness of the thermal boundary layer adjacent to the deforming zone, we can model deformation as slip on a mathematical plane. For this limit, the bulk temperature evolution in the deforming zone is solved for using a Green's function to find [*Carslaw and Jaeger*, 1959]

$$T(t) = T_0 + \int_0^t \frac{\tau(s) V(s)}{\rho c} \frac{1}{\sqrt{4\pi \alpha_{\text{th}}(t-s)}} ds. \quad (9.15)$$

Using the velocity-dependent expression for strength given in equation (9.7) (where as before we neglect the contribution of f_w), we nondimensionalize equation (9.15) to find

$$\tilde{T}(\tilde{t}) = \int_0^{\tilde{t}} \frac{(1 - \tilde{T})^2}{\sqrt{4\pi(\tilde{t} - \tilde{s})}} d\tilde{s}, \quad (9.16)$$

where dimensionless variables are denoted with tildes and we use the scalings $T = T_a + (T_w - T_a)\tilde{T}$ and $t = t_w^{\text{SP}}\tilde{t}$, defining the weakening timescale as

$$t_w^{\text{SP}} = \frac{\alpha_{\text{th}}}{V_{\text{w.gouge}}(T_0)^2} \left(\frac{\rho c (T_w - T_0)}{f_0(\sigma_n - p_0)} \right)^2. \quad (9.17)$$

Equation (9.16) shows that the temperature evolution is of the form

$$T(t) = T_0 + (T_w - T_0)F(t/t_w^{\text{SP}}), \quad (9.18)$$

where $F(\cdot)$ is a nondimensional, monotonically growing function with $F(0) = 0$ and $\lim_{t \rightarrow \infty} F(t) = 1$. An asymptotic analysis of equation (9.16), checked against numerical solutions, shows that

$$T(t) \approx T_0 + (T_w - T_0) \left(1 - \sqrt{2} (\pi t / t_w^{\text{SP}})^{-1/4} \right) \quad (9.19)$$

for $t \gg t_w^{\text{SP}}$. The temperature evolution, and therefore the strength evolution, is controlled by a single characteristic weakening timescale t_w^{SP} given by equation (9.17). Note that as in the solution for adiabatic conditions given in equation (9.11), the temperature evolution in the slip-on-a-plane limit is independent of the exact slip rate history of the fault because the friction coefficient is proportional to $1/V$. Thus, the evolution of V_w is independent of the exact slip rate history of the fault, though the strength evolution of the fault is still sensitive to the slip rate history because the friction coefficient is equal to V_w/V .

For deformation at constant slip rate, the weakening timescale given in equation (9.17) directly translates into a slip weakening distance. For the slip-on-a-plane limit we calculate the fracture energy

$$G_{\text{FH}}^{\text{SP}} = \frac{\tau_c^2 D}{N_c \pi f_0 (\sigma_n - p_0)} \times F'(t/t_w^{\text{SP}}), \quad (9.20)$$

where $F'(\cdot)$ is again a nondimensional, monotonically growing function, but not bounded. F' cannot be determined in closed form, and we use a numerical solution to calculate F' , avoiding further approximations. Nevertheless, based on the asymptotic form (19) for temperature, we can determine the following asymptotic scaling of fracture energy for $t \gg t_w^{\text{SP}}$:

$$G_{\text{FH}}^{\text{SP}}(t) \approx \frac{\tau_c^2 D}{N_c \pi f_0 (\sigma_n - p_0)} \left(2 \sqrt{\frac{t}{\pi t_w^{\text{SP}}}} \right), \quad (9.21)$$

which shows that the leading term at large time is proportional to \sqrt{t} .

9.2.2. Thermal Pressurization of Pore Fluid

Our analysis for thermal pressurization closely follows previous work by *Lachenbruch* [1980], *Mase and Smith* [1985], *Mase and Smith* [1987], *Rice* [2006], and *Rempel and Rice* [2006]. Here we summarize the main results and governing equations, and refer the reader to the aforementioned literature for the details of the model and solutions. We consider a one-dimensional model of a gouge layer with thickness W sheared between two undeforming half-spaces with a slip rate V .

Conservation of energy leads to an equation for T that balances frictional heating and thermal diffusion,

$$\frac{\partial T}{\partial t} = \frac{\tau \dot{\gamma}}{\rho c} + \alpha_{\text{th}} \frac{\partial^2 T}{\partial y^2}, \quad (9.22)$$

where τ is the shear stress in the gouge layer and $\dot{\gamma}$ is the strain rate. Following previous work, we have assumed here that all of the frictional work is converted into heat and that the gouge properties are constant in space and time. In addition, we have neglected small heat fluxes associated with pore fluid flow, which *Mase and Smith* [1985] and *Mase and Smith* [1987] showed is a good assumption for typical fault rock permeabilities.

In a fluid saturated material, the increase in temperature induced by shear heating leads to an increase in pore pressure due to the difference between the thermal expansivities of the fluid and of the rock. Conservation of pore fluid mass leads to an equation for the pore pressure p that balances thermal pressurization and hydraulic diffusion,

$$\frac{\partial p}{\partial t} = \Lambda \frac{\partial T}{\partial t} + \alpha_{\text{hy}} \frac{\partial^2 p}{\partial y^2}, \quad (9.23)$$

where Λ is the ratio of pore pressure rise to temperature rise for undrained conditions and α_{hy} is the hydraulic diffusivity. As before, we have assumed that the gouge properties are constant in space and time. The parameter Λ controls the efficiency of the thermal pressurization process and is defined as

$$\Lambda = \frac{\lambda_f - \lambda_n}{\beta_f + \beta_n}, \quad (9.24)$$

where λ_f and λ_n are the thermal expansion coefficients of the fluid and of the pore space, and β_f and β_n are the compressibilities of the fluid and of the pore space, respectively. The hydraulic diffusivity is expressed as

$$\alpha_{\text{hy}} = \frac{k_f}{n(\beta_n + \beta_f)\eta}, \quad (9.25)$$

where k_r is the permeability of the rock, n is the porosity, and η is the viscosity of the saturating fluid.

The governing equations for temperature and pore pressure are linked to the fault strength τ_{fault} through the Terzaghi effective stress, which combines with the friction coefficient f to give

$$\tau_{\text{fault}} = f(\sigma_n - p_0). \quad (9.26)$$

For simplicity and throughout the remainder of this chapter we assume a constant friction coefficient. This simplification allows us to investigate thermal pressurization independently from flash heating.

To close the model, we need an equation to describe how strain is distributed across the deforming gouge. Previously published models typically choose a fixed spatial distribution of strain rate, the amplitude of which can vary in time [e.g., *Andrews, 2002; Rempel and Rice, 2006; Noda et al., 2009*]. In the spirit of making elementary estimates, we choose a simple model with uniform shear in the deforming zone,

$$\dot{\gamma} = \frac{V}{W} \quad \text{when } |y| < W/2. \quad (9.27)$$

The assumption of a constant deforming zone thickness is likely a great simplification. *Rice et al. [2014]* and *Platt et al. [2014b]* showed that thermal pressurization drives significant strain localization, as first suggested in *Rice [2006]*. However, *Platt et al. [2014b]* showed that while strain localization greatly influences the details of shear strength evolution at large slip, the early stages of slip, for which undrained and adiabatic conditions best apply, remain controlled by the initial imposed thickness W . Therefore, the first-order model based on equation (27) still provides excellent estimates for the efficiency of weakening by thermal pressurization under adiabatic, undrained conditions.

Two well-studied limits exist for thermal pressurization, controlled by the ratio between the thickness of the deforming gouge and the thickness of the diffusive boundary layer that forms adjacent to it. During the early stages of slip, the effects of hydrothermal diffusion are negligible and deformation occurs under effectively undrained and adiabatic conditions. At large slips the diffusive boundary layer is much greater than the deforming zone thickness, allowing deformation to be modeled as slip on a mathematical plane. *Rempel and Rice [2006]* showed that for intermediate slips the shear strength smoothly transitions from the undrained and adiabatic limit to the slip-on-a-plane limit, and thus these two limits can be used to estimate the efficiency of thermal pressurization.

First we analyze the small-slip limit, where thermal pressurization occurs under undrained and adiabatic

conditions. *Lachenbruch [1980]* solved for the shear strength evolution in this limit to find

$$\tau_{\text{fault}} = f(\sigma_n - p_0) \exp\left(-\frac{f\Lambda}{\rho c} \frac{\delta}{W}\right), \quad (9.28)$$

where p_0 is the ambient pore pressure before the onset of rapid slip and δ is the total slip accommodated across the gouge layer, defined as

$$\delta(t) = \int_0^t V(s) ds. \quad (9.29)$$

Equation (9.28) shows that thermal pressurization under undrained and adiabatic conditions is controlled by a critical weakening strain

$$\gamma_c = \frac{\rho c}{f\Lambda}, \quad (9.30)$$

and is insensitive to details of the slip rate history. For sustained slip at high velocity, equation (9.28) predicts a total loss of strength. The existence of a critical strain indicates that the slip required to produce a given amount of weakening scales linearly with the deforming zone thickness, making thermal pressurization most effective when straining is highly localized. The temperature evolution for an undrained adiabatic deformation is given by [*Lachenbruch, 1980*]

$$T = T_0 + \frac{\sigma_n - p_0}{\Lambda} \left(1 - \exp\left[-\frac{f\Lambda}{\rho c} \frac{\delta}{W}\right]\right), \quad (9.31)$$

where T_0 is the ambient temperature before the onset of rapid slip. The total strength drop associated with thermal pressurization leads to a finite maximum temperature rise:

$$\Delta T_{\text{max}}^{\text{UA}} = \frac{\sigma_n - p_0}{\Lambda}. \quad (9.32)$$

Finally, we estimate the fracture energy G by inserting the shear strength given in equation (9.28) into equation (9.1). For deformation under undrained and adiabatic conditions we find that G tends to

$$G_{\text{TP}}^{\text{UA}} = W \frac{\rho c (\sigma_n - p_0)}{\Lambda}. \quad (9.33)$$

for $\delta \gg \delta_c = \gamma_c \times W$. The fracture energy for undrained and adiabatic conditions can be understood physically by noting that $G_{\text{TP}}^{\text{UA}} = f(\sigma_n - p_0)\delta_c$.

Next we analyze the large-slip limit, where deformation can be modeled as slip on a mathematical plane. Assuming a constant slip rate, *Rice* [2006] solved for this limit accounting for hydraulic and thermal diffusion, extending previous work of *Mase and Smith* [1985, 1987] that accounted for thermal or hydraulic diffusion alone, to find the shear strength evolution

$$\tau_{\text{fault}} = f(\sigma_n - p_0) \exp\left(\frac{\delta}{L^*}\right) \operatorname{erfc}\left(\sqrt{\frac{\delta}{L^*}}\right), \quad (9.34)$$

where L^* is a critical weakening slip defined as

$$L^* = \frac{4\alpha}{V} \left(\frac{\rho c}{f\Lambda}\right)^2 \quad (9.35)$$

and $\alpha = (\sqrt{\alpha_{\text{th}}} + \sqrt{\alpha_{\text{hy}}})^2$ is a lumped hydrothermal diffusivity. Similarly to deformation under undrained and adiabatic conditions, thermal pressurization in the slip-on-a-plane limit leads to a total strength drop, though this is now controlled by the critical weakening slip L^* . Analytic solutions do not exist for arbitrary nonconstant slip rate histories, but we expect the shear strength evolution to depend sensitively on the slip rate history. The solutions of *Garagash* [2012] and *Viesca and Garagash* [2015] for self-healing slip pulses driven by thermal pressurization show that if the slip rate is initially high and subsequently drops, as expected during dynamic rupture propagation, hydrothermal diffusion can dominate the evolution of temperature and pore pressure, leading to rapid restrengthening. Nevertheless, equation (9.34) provides a useful end-member estimate for weakening by thermal pressurization at large slip. *Rice* [2006] also provides a closed-form solution for the maximum temperature increase on the sliding surface,

$$\Delta T_{\text{max}}^{\text{SP}} = \left(1 + \sqrt{\frac{\alpha_{\text{hy}}}{\alpha_{\text{th}}}}\right) \frac{\sigma_n - p_0}{\Lambda}. \quad (9.36)$$

As for deformation under undrained and adiabatic conditions, the total strength drop associated with thermal pressurization leads to a finite temperature rise. Finally, to estimate the fracture energy we use the asymptotic expression from *Rice* [2006],

$$G_{\text{FH}}^{\text{SP}}(\delta) \approx f(\sigma_n - p_0) \sqrt{(\delta L^*) / \pi}, \quad (9.37)$$

which is valid when $\delta \gg L^*$. In contrast with thermal pressurization operating under undrained and adiabatic conditions, the fracture energy in the slip on plane limit is unbounded at large slip. Equation (9.37) shows that the

fracture energy is proportional to the initial shear strength $f(\sigma_n - p_0)$ multiplied by a length found by taking the geometric mean of the characteristic weakening slip L^* and the total slip δ .

9.3. PARAMETER VALUES AND GEODYNAMIC SETTINGS

As observed above, the efficiency of flash heating and thermal pressurization depends on a number of parameters that vary with rock type, stress, pore pressure, and temperature. In this section we describe how we estimate these parameters and present a selection of ambient temperature and stress profiles for continental, oceanic, and subduction faults.

Not all parameters have the same impact on the final results. Therefore, we use relatively precise values and include temperature and pressure dependencies only for those that provide key controls on the weakening processes. For flash heating, we account for variation of both mechanical (asperity yield strength) and thermal parameters (heat capacity and diffusivity). For thermal pressurization, we account for variations in all the parameters entering into the thermal pressurization factor Λ and the hydraulic diffusivity α_{hy} .

Unfortunately, several important parameters are only loosely constrained (for example, the weakening temperature T_w and the pore pressure distribution at depth), and we therefore choose representative estimates rather than arbitrary specific values.

9.3.1. Flash Heating: Yield Strength and Thermal Properties

Because flash heating is largely controlled by asperity-scale thermal and mechanical parameters, we use parameters associated with individual minerals rather than bulk ones. Here, we use thermal and strength data for two major rock-forming minerals, quartz and olivine, which will serve as representative minerals for the continental and oceanic (both in place and subducted) crust, respectively. Note that our model for the evolution of fault temperature involves thermal parameters related to the bulk; for simplicity, we assume that the bulk properties take the same values as the asperity-scale properties.

Thermal conductivity (k_p) and heat capacity (ρc) data as a function of temperature for both quartz and olivine are taken from *Clauser and Huenges* [1995], and the data are interpolated with cubic splines to produce smoothly varying functions. For quartz, *Clauser and Huenges* [1995] provide data for two crystallographic orientations, and we use the arithmetic average of these data at each temperature.

The stress at asperity contacts is given by

$$\tau_c \approx f \times \sigma_A, \quad (9.38)$$

where f is a microscopic friction coefficient and σ_A the asperity yield stress. We use $f = 0.6$ and σ_A values derived from hardness measurements as a function of temperature taken from *Evans and Goetze* [1979] (for olivine) and *Evans* [1984] (for quartz). For each mineral, the yield strength data are fitted with a second order polynomial to produce regular functions of temperature. The yield strength σ_A typically ranges from 2 to 5 GPa in olivine and from 7 to 13 GPa in quartz, between room temperature and 750°C.

The weakening temperature T_w corresponds to the threshold temperature above which an asperity loses its strength. It is generally associated with the melting temperature or thermal decomposition temperature, which varies from mineral to mineral [e.g., *Rempel and Weaver*, 2008]. However, the precise mechanisms responsible for strength loss are not clear and do not necessarily correspond to conventional melting: minerals like quartz can be amorphized and form a gel [*Goldsby and Tullis*, 2002], and large concentrated strains can influence the melting temperature. Due to the large uncertainties, we follow here the approach of *Goldsby and Tullis* [2011] and assume a constant $T_w = 1000^\circ\text{C}$ as an approximate weakening temperature.

A key parameter in the flash heating model is the diameter of microscale asperities D . In experimental studies, this parameter is often used as a fitting parameter with typical values of a few to tens of microns, but so far it has not been measured directly. Here we estimate how D depends on temperature and stress by modeling how the highly stressed contacts yield. In this approach we assume that the number of contacts remains the same with increasing stress, and that only the surface area of the contact changes. Following the method used by *Boettcher et al.* [2007] and *Hirth and Beeler* [2015], we compute D from the ratio of the real to nominal area of contact between the two rock surfaces, which is given by the ratio of the applied effective normal stress to the asperity yield strength (see *Scholz* [2002]):

$$\frac{A_R}{A} = \frac{\sigma_n - p_0}{\sigma_A}, \quad (9.39)$$

where A_R and A are the real and nominal area of contact per asperity, respectively. Inserting $A_R = \pi D^2/4$ into equation (9.39) yields

$$D = D_0 \sqrt{\frac{\sigma_n - p_0}{\sigma_A}}, \quad (9.40)$$

where $D_0 = \sqrt{4A/\pi}$ is a prefactor with dimension of length. Experimental results for flash heating between bare rock surfaces [*Goldsby and Tullis*, 2011; *Passelègue et al.*, 2014] indicate D values of the order of 10 μm at normal stresses of a few MPa at room temperature, which yields D_0 values of the order of 200 μm .

9.3.2. Thermal Pressurization: Thermal and Hydraulic Properties

The efficiency of thermal pressurization depends on the hydraulic and thermal properties of the fault rock, as well as thermodynamic properties of the pore fluid. Here we are interested in essentially three different fault zone lithologies: one representative of a fault hosted in the igneous continental crust (e.g., granite), one for a mature, gouge-bearing crustal fault, and one for faults hosted in the oceanic crust (the same lithology is used for both in place and subducted oceanic crust). In all these cases we assume that the pore fluid is pure water and neglect any compositional effects on water properties.

Estimating the thermo-poro-elastic parameters λ_n and β_n used to compute the thermal pressurization factor Λ (equation (9.24)) requires some assumptions about the fault stresses (see discussion in *Rice* [2006], Appendix A). We follow here the hypothesis that the fault walls behave elastically, for which *Rice* [2006] gives the following expressions for the pore space compressibility and thermal expansivity:

$$\beta_n = \frac{(\beta_d - \beta_s)(\beta_d + r\beta_s)}{n(1+r)\beta_d} - \beta_s, \quad \lambda_n = \lambda_s \left(1 - \frac{r}{(1+r)} \frac{\beta_d - \beta_s}{n\beta_d} \right), \quad (9.41)$$

where β_d is the drained compressibility of the rock, β_s and λ_s are the compressibility and thermal expansivity of the solid skeleton, respectively, and λ_s is a function of the drained Poisson's ratio of the rock. Following *Rice* [2006] we choose $r = 1$, which corresponds to a drained Poisson's ratio of 0.20. The estimates given in equations (9.41) are not valid for very large pore pressure and temperature rises (i.e., for large slip), since they lead to unsustainable differential stresses on the fault walls [*Rice*, 2006, Appendix A2]. Here, we are interested in stages of seismic slip where the pore pressure has not yet reached elevated values close to σ_n , and it is therefore reasonable to assume that the deformation around the fault core remains elastic.

For the case of faults hosted in igneous rocks, we choose compressibility values measured in sheared granitic gouge by *Zhang et al.* [1999]. The drained β_d was computed from the fault zone thickness vs. effective stress data, and is $\beta_d = \beta_s + 1.1 \times 10^{-9} \exp(-(\sigma_n - p_0)/p_\beta)$ Pa^{-1} , where $p_\beta = 45.5$ MPa. We add the term β_s to ensure

that the drained compressibility of the rock does not fall below the compressibility of the solid grains, and thus β_n remains positive. The compressibility of solid grains is taken as that of a granitic composition and is $\beta_s = 1.6 \times 10^{-11} \text{ Pa}^{-1}$, as in *Rice* [2006]. For gouge, we use the drained compressibility measured by *Wibberley and Shimamoto* [2003] and reported by *Rice* [2006] as $\beta_d = \beta_s + 1.39 \times 10^{-10} \exp(-(\sigma_n - p_0)/p_\beta) \text{ Pa}^{-1}$, where $p_\beta = 144.7 \text{ MPa}$. The compressibility of the solid is generally much lower than the compressibility of the fluid β_f , so that our regularization of β_d using the additional β_s term has no quantitative impact at high effective pressure but provides a natural lower limit on compressibility at low effective pressure.

For all cases, the thermal expansivity of the solid particles is taken as $\lambda_s = 2.45 \times 10^{-5} \text{ }^\circ\text{C}^{-1}$. The thermal expansivity of the pore space is in general smaller than that of the pore fluid, so that the variations in λ_s arising from the range of modeled lithologies and pressure and temperature conditions do not produce significant changes in the thermal pressurization factor Λ .

The properties of the pore fluid, assumed to be pure water, vary widely as a function of pressure and temperature. The two key parameters, thermal expansivity λ_f and compressibility β_f , decrease with increasing pressure and increasing temperature. We compute the pore fluid thermal expansivity, compressibility, and viscosity as a function of p and T using the formulation given by the International Association for the Properties of Water and Steam [*Wagner and Pruß*, 2002; *Junglas*, 2009].

The permeability of fault rocks generally depends on effective stress according to an exponential relation. For igneous rocks, we use the permeability values measured in sheared granitic rocks [*Zhang et al.*, 1999], which yield $k_f = 10^{-19} \exp(-(\sigma_n - p)/p_k) \text{ m}^2$, where $p_k = 357.1 \text{ MPa}$. For gouge, we use the permeability measured in the central gouge zone of the Median Tectonic Line (Japan), reported by *Rice* [2006] as $k_f = 2.12 \times 10^{-19} \exp(-(\sigma_n - p)/p_k) \text{ m}^2$, where $p_k = 34.7 \text{ MPa}$.

The porosity of the rock within the central slip zone is computed as a function of the effective normal stress. For all cases except the clay-rich gouge, we use a porosity of $n = 0.05 \times [1 + \exp(-(\sigma_n - p)/p_n)]$ with $p_n = 45.5 \text{ MPa}$, estimated from the dilation vs. pressure data given by *Zhang et al.* [1999]. For the clay-rich gouge, we use an exponential fit to the values reported by *Rice* [2006], which yields $n = 0.06 \times \exp(-(\sigma_n - p)/p_n)$ with $p_n = 263.2 \text{ MPa}$.

The thermal diffusivity plays a less prominent role in the thermal pressurization model than in the flash heating model. Therefore, for the thermal pressurization computations we chose an average, constant value of $\alpha_{th} = 1 \text{ mm}^2 \text{ s}^{-1}$. Similarly, the heat capacity is assumed constant and equal to $\rho c = 2.7 \text{ MPa } ^\circ\text{C}^{-1}$ [see *Vosteen and Schellschmidt*, 2003].

All the above properties vary during slip as the pore pressure and temperature rise. However, the models presented in section 9.2 are only valid for constant parameter values. Here, we want to retain the essential features of the model while accounting for the variations in properties with pressure and temperature. To achieve this goal, we compute *path-averaged* properties based on the approach proposed by *Rice* [2006]. First, for each scenario (ambient temperature, pressure, and rock type) we compute *nominal* properties using the conditions at the onset of seismic slip. Second, we use the nominal properties to predict the pore pressure and temperature path as a function of slip using either the adiabatic and undrained or the slip on plane scenario. Finally, we compute path averaged properties using slip as the weight function:

$$\langle X \rangle = \frac{1}{\delta} \int_0^\delta X[p(\delta'), T(\delta')] d\delta', \quad (9.42)$$

where $\langle X \rangle$ is the path averaged value of $X(p, T)$ and δ is slip. The net slip over which equation (9.42) is computed is either set to δ_c in the case of adiabatic, undrained computations or to L^* in the case of slip-on-a-plane computations. Thus, for each scenario we produce two values of α_{hy} and Λ , one thought to best describe the early stages of weakening and another that describes the weakening at larger slips.

In all thermal pressurization computations, we choose a constant slip rate of $V = 1 \text{ m s}^{-1}$, which is commonly used as a typical seismic slip rate [e.g., *Brune*, 1970]. The relevant friction coefficient at this slip rate is potentially affected by the flash heating mechanism. *Rice* [2006] and *Rempel and Rice* [2006] assumed reduced values of friction, as low as 0.25, to approximate the nearly-instantaneous effect of flash heating. However, this approach may not be valid for deforming gouge where flash heating is less effective because the effective critical weakening velocity is multiplied by the number density of contacts in the gouge width (typically at least a factor of $N_c = 10$). Therefore, we choose here a ‘‘Byerlee’’-type friction coefficient of $f = 0.6$, allowing us to study thermal pressurization in isolation. This choice of a relatively high value of f implies that our results will be upper bounds for the efficiency of thermal pressurization (i.e., lower bounds for γ_c and L^*).

9.3.3. Thermal and Effective Stress Profiles

We investigate the dynamic weakening behavior of faults within three major geodynamic settings: active continental crust (where we use either clay-bearing or crushed granite as fault gouge material), near-ridge oceanic crust (which hosts oceanic transform faults), and subduction zones. The key difference between these

settings is the local geotherm, and to a lesser extent the lithostatic and hydrostatic stress profile.

Geotherms in tectonically active regions of the continental crust are quite variable, especially in their deepest parts [Jaupart and Mareschal, 2007]. Here we focus on the shallow seismogenic crust (typically above the 600°C isotherm), where surface heat flow measurements, together with estimates of radiogenic heat production, provide a solid estimate of temperature profiles. We follow a standard model using an exponential decay of radiogenic heat production with depth over a characteristic distance $h_r = 10$ km, so that the temperature profile is given by Turcotte and Schubert [2002]:

$$T_0(z) = T_{\text{surface}} + \frac{A_0 h_r^2}{k_{\text{crust}}} (1 - e^{-z/h_r}) + \frac{(q - A_0 h_r)z}{k_r}, \quad (9.43)$$

where we use a surface temperature $T_{\text{surface}} = 13^\circ\text{C}$, an average thermal conductivity of $k_{\text{crust}} = 3 \text{ W }^\circ\text{C}^{-1} \text{ m}^{-1}$ [Chapman, 1986; Jaupart and Mareschal, 2007], a nominal rate of internal energy production of $A_0 = 2 \mu\text{W m}^{-3}$ [Turcotte and Schubert, 2002], and a surface heat flux of $q = 80 \text{ mW m}^{-2}$ (based on heat flow measurements near the San Andreas fault, from Lachenbruch and Sass [1980]). We use an average rock density of 2800 kg m^{-3} to compute the lithostatic stress profile. The ambient pore pressure is assumed hydrostatic, and we calculate the ambient pore pressure profile using a pore pressure gradient of 9.8 MPa km^{-1} . This pressure gradient is based on a constant fluid density: the assumption of a hydrostatic pore fluid pressure at depth is a relatively strong one, and a detailed model including water density variations appears unnecessary at this stage.

The thermal structure of the oceanic crust is much better constrained than that of the active continental crust. It is well approximated by a cooling plate model, which is a function of the age of the crust [e.g., Turcotte and Schubert, 2002]: $T_0(z) = T_M \text{erf}\left(z / \left(2\sqrt{k_T t_{\text{crust}} / \rho c}\right)\right)$, where T_M is the mantle temperature, set to $T_M = 1350^\circ\text{C}$, z is the depth, and t_{crust} is the age of the crust. For our calculations we used a heat conductivity of $k_T = 3.14 \text{ W }^\circ\text{C}^{-1} \text{ m}^{-1}$ [Parsons and Sclater, 1977], and a crustal age of 1.25 My, which corresponds to a relatively young oceanic crust hosting an oceanic transform fault. The normal stress and pore pressure profiles in the oceanic crust are computed using a rock density of 3200 kg m^{-3} and a pore pressure gradient of 9.8 MPa km^{-1} . In addition, we considered a water depth above the crust of 2 km, which offsets both the ambient normal stress and pore pressure values by 20 MPa.

Finally, for the thermal profile of the subduction settings we assume a linear gradient of 6°C km^{-1} , which corresponds to a relatively cold subduction (e.g., Tohoku

or Nankai; see Hacker *et al.* [2003]). The rock density used to compute the lithostatic stress is 3200 kg m^{-3} , and we assume a water depth above the crust of 10 km, which offsets the normal stress and pore pressure by 100 MPa. In subduction zones, dehydration reactions of hydrous phases at depth tend to promote elevated pore pressures along the subduction interface [e.g., Peacock *et al.*, 2011]. We therefore tested two ambient pore pressure profiles, one hydrostatic (9.8 MPa km^{-1}) and another with elevated (near lithostatic) pore pressures (27.6 MPa km^{-1}), which corresponds to a pore pressure-to-lithostatic pressure ratio of 0.9.

9.4. DEPTH- AND CONTEXT-DEPENDENT DYNAMIC WEAKENING PROFILES

In this section we combine the parameter choices justified in section 9.3 with the models developed in section 9.2 to predict how the efficiency of dynamic weakening varies within the seismogenic zone. To begin, we analyze flash heating and thermal pressurization individually, then compare these results to predict how the dominant weakening mechanisms changes with depth.

9.4.1. Flash Heating

The critical weakening velocity $V_{w,\text{gouge}}$ and characteristic weakening times t_w^A and t_w^{SP} for flash heating are plotted as a function of depth in Figure 9.1. In all cases, $V_{w,\text{gouge}}$ decreases with increasing depth. In the continental crust, based on quartz mineral data, $V_{w,\text{gouge}}$ decreases from around 1 ms^{-1} in subsurface conditions down to less than 0.1 ms^{-1} at 20 km depth, near the 600°C isotherm. The critical weakening velocities computed from olivine data are higher than those computed from quartz data due to the lower asperity strength τ_c , and typically are of a few ms^{-1} at the top of the oceanic crust and subduction zones, and decrease by a factor of around 5 at 6 km and 50 km depth, respectively. For near-lithostatic pore pressure gradients (dashed lines in Figure 9.1c), $V_{w,\text{gouge}}$ is offset toward higher values because the lower effective stresses induce lower asperity contact sizes D (see equation [9.40]).

The characteristic weakening times t_w^A and t_w^{SP} tend to either decrease or remain constant with increasing depth. In the continental crust, both these times remain of the order of 10^{-2} s: t_w^A is approximately constant throughout the profile, while t_w^{SP} first decreases from around 5×10^{-2} s to 10^{-2} s in the top 10 km, and then remains nearly constant below. By contrast, in both oceanic and subduction environments the weakening times monotonically decrease with increasing depth. In our modeled oceanic transform fault, t_w^A and t_w^{SP} are both of the order of 10^{-2} s near the top of the crust, and decrease down to $t_w^A = 1.8 \times 10^{-3}$ s and $t_w^{\text{SP}} = 3.6 \times 10^{-4}$ s at 6 km depth. Similarly, in the modeled

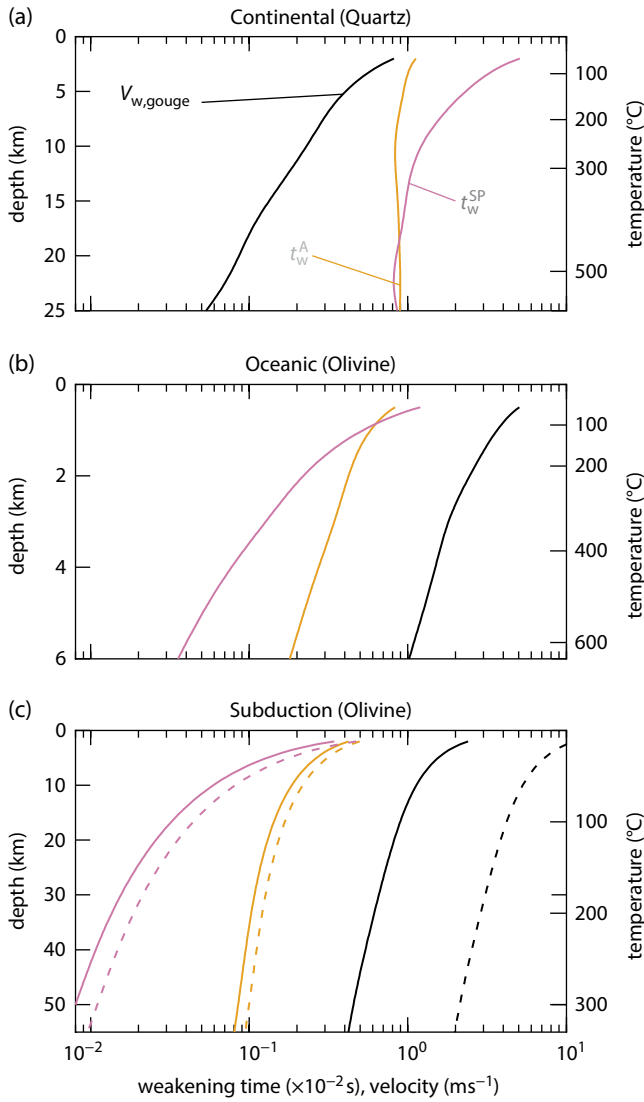


Figure 9.1 Critical weakening velocity and weakening times for the flash heating mechanism, in continental (a), oceanic (b) and subduction (c) settings. The weakening time for adiabatic conditions t_w^A is computed using $W = 100 \mu\text{m}$. The solid and dashed lines in panel (c) correspond to hydrostatic and near-lithostatic pore pressure gradients, respectively. See *electronic version for color representation*.

subduction zone, t_w^A decreases from 4.2×10^{-3} s to 8.0×10^{-4} s between subsurface and 55 km depth, while t_w^{SP} drops from 3.4×10^{-3} s to 7.0×10^{-5} s over the same depth range. The change between hydrostatic and near-lithostatic pore pressure gradients does not affect the weakening times significantly, only by about 15% to 30%.

For comparison, we performed additional computations using a constant asperity size $D = 10 \mu\text{m}$, shown in Figure 9.2, which correspond to scenarios where the increase in real area of contact with effective normal stress is only due to an increase in the number of contacts.

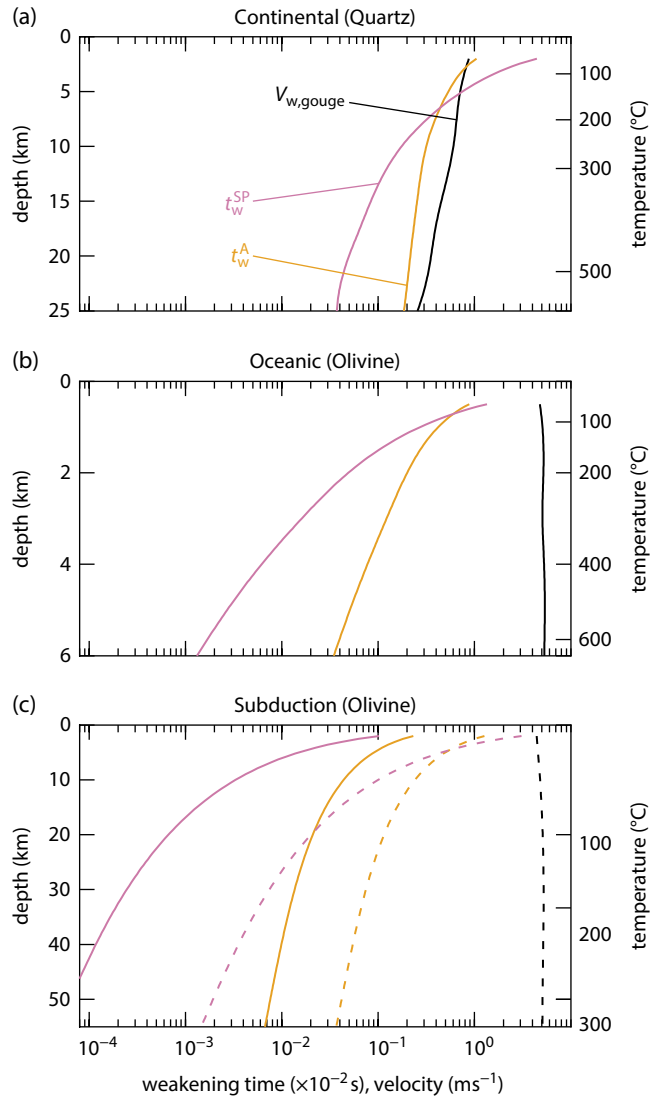


Figure 9.2 Critical weakening velocity and weakening times for the flash heating mechanism assuming constant asperity diameter $D = 10 \mu\text{m}$, in continental (a), oceanic (b) and subduction (c) settings. The weakening time for adiabatic conditions t_w^A is computed using $W = 100 \mu\text{m}$. The solid and dashed lines in panel (c) correspond to hydrostatic and near-lithostatic pore pressure gradients, respectively. See *electronic version for color representation*.

These complementary tests show that the weakening velocity decreases only mildly or remains constant with increasing depth, while both weakening times decrease much more strongly compared to the case with variable D . These observations are consistent with the increase in contact size D with increasing depth, as computed from equation (9.40), and shown in Figure 9.3. If the increase in true contact area with increasing normal stress is accommodated by a combination of growing existing contacts and form new contacts, then the true depth dependence of flash heating likely lies between the two end-members shown in Figures 9.1 and 9.2.

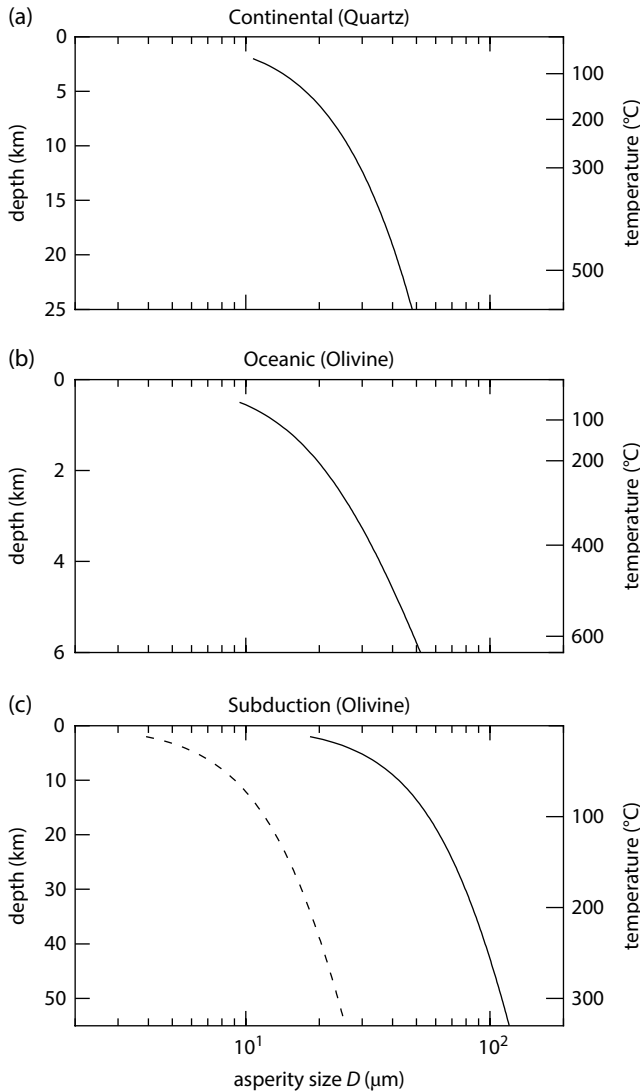


Figure 9.3 Asperity contact size D as a function of depth in continental (a), oceanic (b) and subduction (c) settings, as computed from equation (9.40). Solid lines correspond to hydrostatic pore pressure gradients, and dashed line (in subplot [c]) corresponds to sublithostatic pore pressure gradients.

Overall, our results show that flash heating typically becomes more efficient with increasing depth, with lower critical weakening velocities and shorter weakening times. Temperature changes tend to reduce the weakening velocity and produce weakening in the first 10^{-4} to 10^{-1} s of slip. The decrease in $V_{w, \text{gouge}}$ with depth is essentially due to the decrease in the difference between ambient and weakening temperatures ($T_w - T_0$). However, the decrease in ($T_w - T_0$) with depth is somewhat compensated for by the concomitant decrease in yield stress σ_A and increase in heat diffusivity, so that the net change in V_w (and hence in $V_{w, \text{gouge}}$) is rather moderate.

Our modeling results are qualitatively consistent with the experimental data of *Proctor et al.* [2014], which show

a more abrupt weakening with increasing normal stress. However, our results differ slightly from those of *Passelègue et al.* [2014], who showed a modest increase in V_w with increasing ambient temperature from room temperature to 300°C. A number of factors can explain this discrepancy, the major one being the sensitivity of the results to slight changes in σ_A and heat conductivity. In addition, the calculations of *Passelègue et al.* [2014] did not account for changes in asperity size, which tend to decrease the weakening velocity at increasing temperatures. Despite these uncertainties, we expect that the strong sensitivity of V_w to T_0 , as shown in equation (9.5), overtakes other possibly counteracting effects at high temperatures.

9.4.2. Thermal Pressurization

The efficiency of thermal pressurization relies heavily on the thermal pressurization factor Λ , which combines the thermo-poro-elastic properties of the fault rock and of the pore fluid. Depth profiles of Λ are shown in Figure 9.4. For each setting and rock type, two path-averaged values of Λ are given, one corresponding to the undrained, adiabatic limit (u.a.), and the other to the slip-on-a-plane limit (s.p.). In Figure 9.4, dashed parts of the curves indicate that the peak temperature (computed using equations [9.32] and [9.36]) during thermal pressurization exceeds 1100°C, which is taken as a representative bulk melting temperature.

For a fault hosted in the continental crust (Figure 9.4a), Λ is typically low near the surface: between 0.23 and 0.30 MPa °C⁻¹ in the granite gouge and between 0.44 and 0.58 MPa °C⁻¹ in the clay-rich gouge. Λ increases with increasing depth and reaches a maximum at depths between 8 and 13 km, below which it decreases again. In the undrained, adiabatic limit, Λ peaks at 0.81 MPa °C⁻¹ in the clay-rich gouge and at 0.97 MPa °C⁻¹ in the granite gouge. In the slip-on-a-plane limit, the peak in Λ is less marked (around 0.6 and 0.7 MPa °C⁻¹ for the granite and clay-rich gouge, respectively) and at shallower depths. The evolution of Λ with depth in our modeled oceanic crust is qualitatively similar to that in the continental crust (Figure 9.4b): Λ is relatively small near the surface (between 0.1 and 0.2 MPa °C⁻¹), increases with depth up to a peak (around 0.5 MPa °C⁻¹ at depths between 2 and 4 km), and then decreases in deeper parts of the crust. In the subduction zone setting with hydrostatic pore pressure gradient (Figure 9.4c, black curves), Λ increases very markedly with depth and reaches values between 1.5 and 2.4 MPa °C⁻¹ at depths ranging from 20 to 35 km. By contrast, under near-lithostatic pore pressure conditions (gray curves), the increase in Λ is less pronounced, and both estimates (undrained adiabatic and slip on a plane) yield similar values reaching around 0.6 MPa °C⁻¹ at 50 km depth.

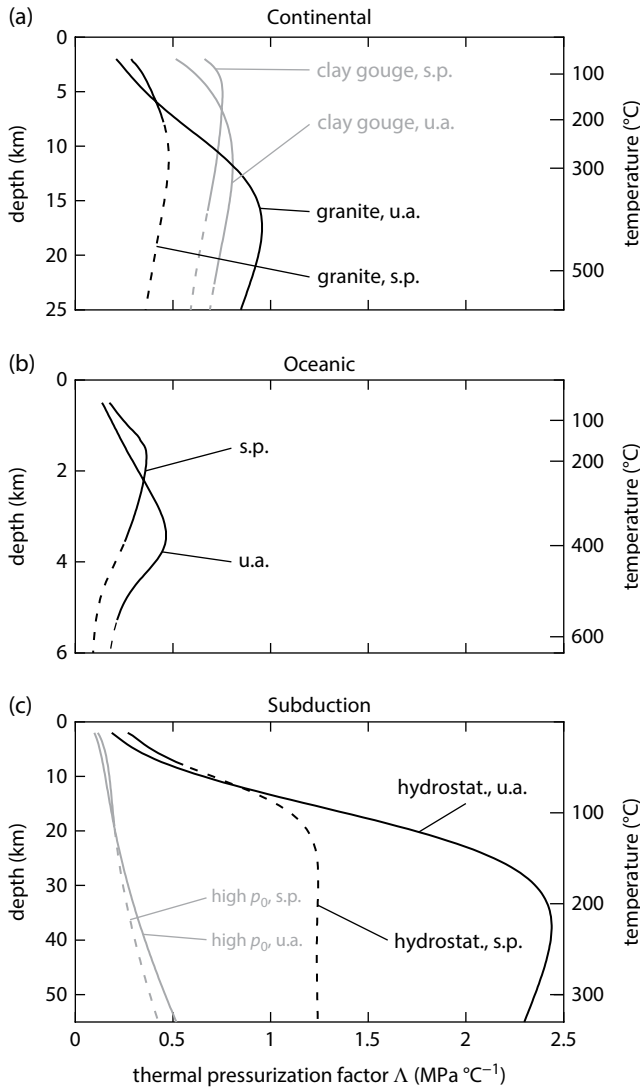


Figure 9.4 Path-averaged value of the thermal pressurization factor Λ as a function of depth for continental (a), oceanic (b), and subduction (c) environments. For every case, two estimates are given: one for the slip-on-a-plane path (s.p.) and one for the undrained, adiabatic path (u.a.). Dashed sections of the curves corresponds to cases when the peak temperature during thermal pressurization is beyond 1100°C , which is chosen as the bulk melting point.

The evolution in Λ is essentially linked to the change in thermodynamic properties of water with pressure and temperature. This is illustrated in Figure 9.5, which compares Λ and the ratio λ_r/β_f (i.e., the thermal pressurization factor that would be obtained if the rock was incompressible). With increasing depth, both λ_r and β_f tend to increase, but β_f increases faster so that the ratio λ_r/β_f tends to decrease. In the shallow parts of the crust, Λ is significantly lower than λ_r/β_f because the pore space has a high compressibility, but the difference decreases

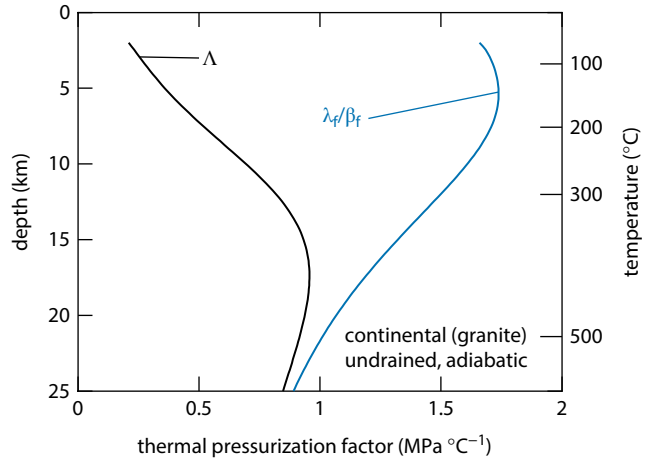


Figure 9.5 Comparative evolution of the thermal pressurization factor Λ and the ratio λ_r/β_f with depth. This example corresponds to the continental geotherm, granite gouge properties, and values obtained from the undrained, adiabatic path. See electronic version for color representation.

with increasing depth owing to the pressure-dependency of the pore space compressibility. The peak in Λ occurs when the increase in β_f compensates the decrease in β_n with increasing depth.

The other key parameter controlling thermal pressurization is the hydraulic diffusivity α_{hy} . Figure 9.6 summarizes the path-averaged diffusivity profiles for the continental, oceanic, and subduction contexts. For the clay-rich gouge material, the hydraulic diffusivity decreases markedly with increasing depth. In all other cases, the hydraulic diffusivity tends to remain constant (in the oceanic context) or increase with depth. Such an evolution is explained by comparing the pressure sensitivity of permeability to the pressure (and temperature) sensitivity of the storage capacity $n(\beta_n + \beta_f)$: the permeability of the clay-bearing gouge decreases strongly with effective pressure (small value of p_k), whereas both the porosity and pore compressibility depend only moderately on pressure (relatively large values of p_β and p_n). By contrast, the permeability of the granitic gouge (chosen in all other scenarios) exhibits a rather moderate pressure sensitivity (large p_k), while both the porosity and compressibility decrease more strongly with pressure (small p_β and p_n). In all cases, the decrease in fluid viscosity η_f with increasing temperature also contributes to increase the hydraulic diffusivity at depth.

Based on the path-averaged values of Λ , α_{hy} , and the remaining parameters, we compute estimates of the critical weakening strain γ_c and critical slip L^* . Figure 9.7 shows a series of profiles for the three representative settings. In all cases, the evolution in γ_c clearly mirrors the evolution in Λ , and exhibits a minimum at midcrustal depths. In the continental setting, γ_c ranges from 10 to 20

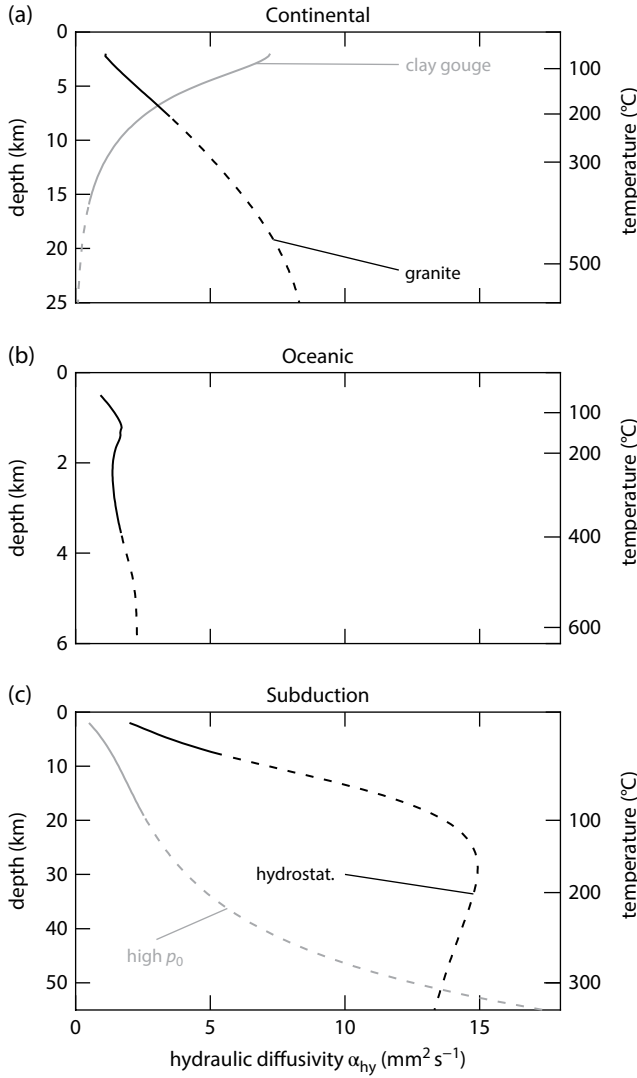


Figure 9.6 Profiles of the path-averaged hydraulic diffusivity α_{hy} in continental (a), oceanic (b), and subduction (c) settings. Dashed parts of each curve correspond to depths at which the peak temperature during thermal pressurization is above 1100°C.

near the surface and decreases to a minimum of around 5 at around 10 km depth. In the oceanic setting, γ_c follows a qualitatively similar evolution, with a shallow maximum around 30, and a midcrustal minimum of around 10. In the subduction setting, γ_c monotonically decreases from shallow to deep parts by a factor of 10 and 7 for hydrostatic and near-lithostatic pore pressure gradients, respectively. The depth profiles of L^* typically follow the profiles of γ_c at shallow depth, but L^* tends to remain small in deeper parts of the crust. The magnitude of L^* ranges between 0.5 and 15 mm, with the smallest values corresponding to the clay-rich gouge (which has a low hydraulic diffusivity).

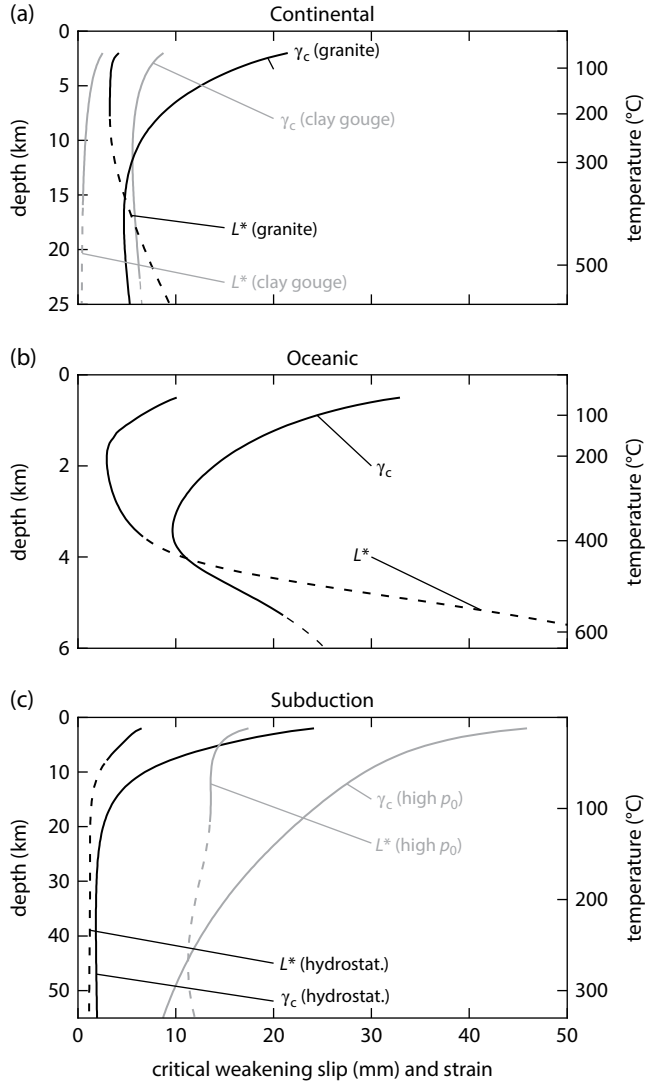


Figure 9.7 Profiles of the critical weakening strain γ_c and slip L^* in continental (a), oceanic (b), and subduction (c) settings. Dashed parts of each curve correspond to depths at which the peak temperature during thermal pressurization is above 1100°C.

9.4.3. Relation to Earthquake Dynamics

Overall, our computations of γ_c and L^* show that the efficiency of thermal pressurization increases with depth, reaching a peak at midcrustal depths. Flash heating is also more efficient with increasing depth, with decreasing critical weakening velocity and weakening times.

A more integrated estimate of the impact of thermal pressurization and flash heating on earthquake propagation is the fracture energy, which measures the energy required to advance the rupture front during an earthquake. As noted in section 9.2, some fracture energy estimates for flash heating and thermal pressurization

have an explicit dependence on total slip. For simplicity, we arbitrarily fix the slip at 1 m, which is representative of an Mw 6 earthquake. This allows us to easily compare the trends for fracture energy evolution vs. depth.

Figure 9.8 shows the profiles of G_{TP}^{UA} and G_{TP}^{SP} , computed using a total slip of $\delta = 1$ m. For a shear zone width of $W = 100 \mu\text{m}$, G_{TP}^{UA} typically increases from around 2×10^{-2} to $2 \times 10^{-1} \text{ MJ m}^{-2}$ from shallow to deep parts of all our modeled settings. Remarkably, most profiles exhibit a minimum or at least a plateau at midcrustal depths, which reflects the existence of a peak in Λ at these depths. In the slip-on-a-plane limit, the computed fracture energy G_{TP}^{SP} also increases with increasing depth, with values ranging from around 3×10^{-1} to around 5 MJ m^{-2} in the deepest sections.

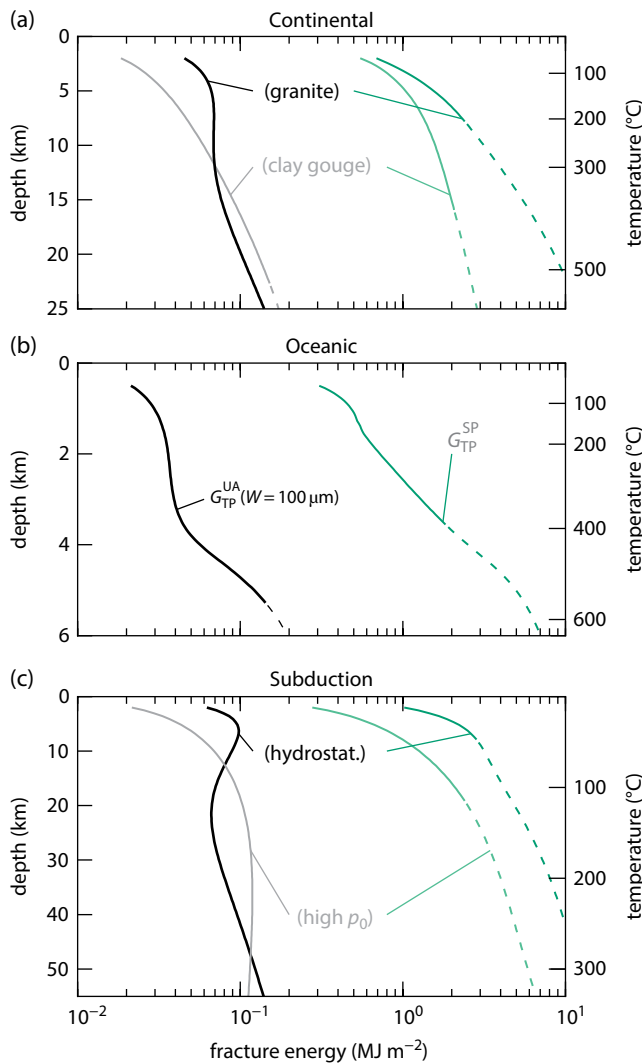


Figure 9.8 Profiles of fracture energy from thermal pressurization in the undrained, adiabatic limit (G_{TP}^{UA} , black and grey curves, computed using $W = 100 \mu\text{m}$) and slip-on-a-plane limit (G_{TP}^{SP} , green curves), computed at $\delta = 1$ m slip, in continental (a), oceanic (b) and subduction (c) settings. See *electronic version for color representation*.

By contrast, the values of fracture energy computed from the flash heating mechanism, shown in Figure 9.9, generally remain constant or slightly decrease with increasing depth. Under adiabatic conditions, weakening by flash heating due to thermal effects corresponds to a fracture energy of the order of $10^{-1} \text{ MJ m}^{-2}$, with little variation (no more than a factor of 2) with depth in all our modeled settings. In the slip-on-a-plane limit, the fracture energy exhibits a similar trend, but at average values of the order of 1 MJ m^{-2} . The inferred range between 1 and 10 MJ m^{-2} is well within the observed

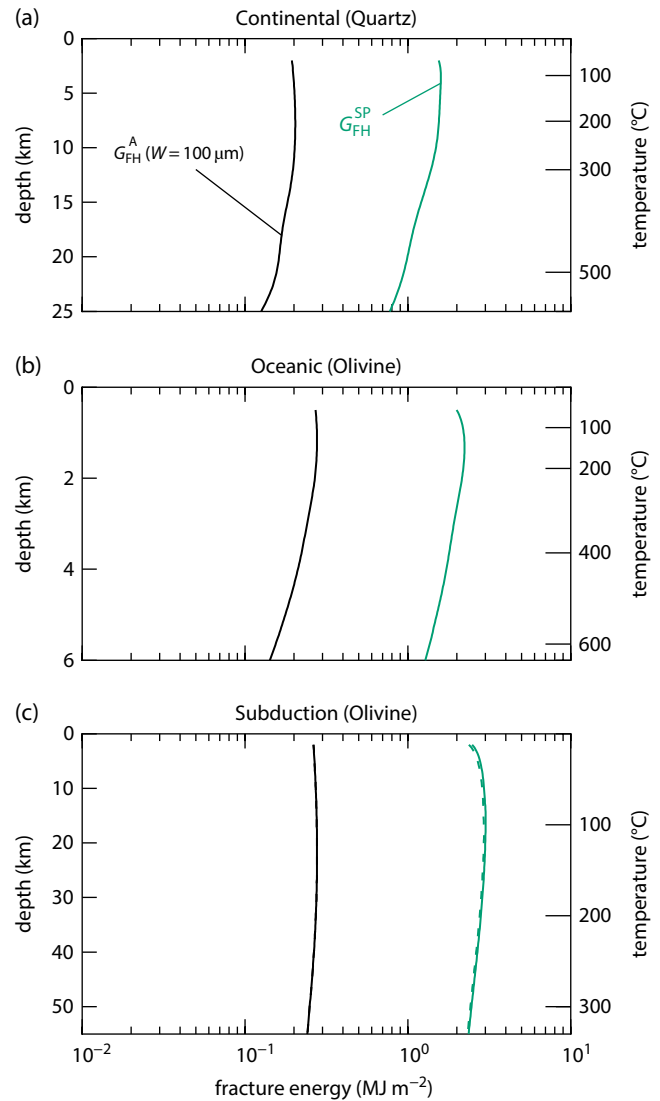


Figure 9.9 Profiles of fracture energy from flash heating in the adiabatic limit (G_{FH}^A , black curves, computed using $W = 100 \mu\text{m}$) and slip-on-a-plane limit (G_{FH}^{SP} , green curves), computed at $\delta = 1$ m slip, in continental (a), oceanic (b) and subduction (c) settings. Solid lines correspond to hydrostatic pore pressure gradients, and dashed line (in subplot [c]) corresponds to sublithostatic pore pressure gradients. See *electronic version for color representation*.

range for earthquakes associated with a few meters of slip [Viesca and Garagash, 2015].

The comparison between fracture energies computed for weakening by thermal pressurization and flash heating in each limit (adiabatic/undrained or slip on a plane) shows that thermal pressurization tends to correspond to lower fracture energies at shallow depths, typically in the top 5 km, and is hence expected to be the dominant weakening process (at least for ruptures with slip of a few meters). In deeper parts of faults, flash heating becomes more efficient (essentially due to a decrease in the asperity yield stress and the proximity of the ambient temperature to the weakening temperature) and produces lower fracture energies than thermal pressurization. Furthermore, especially in the slip-on-a-plane limit, thermal pressurization tends to induce unreasonably large maximum temperature rises (beyond the bulk melting point; see dashed parts of curves in Figure 9.8). If the bulk melting temperature is reached, the model of thermal pressurization becomes invalid and different physical processes need to be accounted for. In some rock types, thermal decomposition might also occur, buffering the local temperature and providing another source of fluid pressure [e.g., Sulem and Famin, 2009; Brantut et al., 2010, 2011].

Figures 9.8 and 9.9 were obtained assuming a total slip distance of 1 m; however, for both mechanisms, flash heating and thermal pressurization, fracture energy tends to increase with slip. Figure 9.10 is a plot illustrating how fracture energy evolves across a wide range of slip distances, taken at depths of 3 km (left) and 10 km (right) in the case of continental crust. The curves for thermal

pressurization (in black) essentially reproduce the results from Rice [2006], showing an increase in G as $\delta^{1/2}$ for large slip (in the slip-on-a-plane limit), and another scaling as δ^2 at small slip (in the adiabatic, undrained limit) [Viesca and Garagash, 2015]. Similarly, for flash heating, the adiabatic limit shows a scaling of G as t^2 , which leads to $G \propto \delta^2$ at constant slip rate. For longer time (or slip) scales, in the slip-on-a-plane limit, the fracture energy associated with flash heating shows a milder scaling, with a slip exponent approaching 1/2 (see equation [9.21]). Figure 9.10 clearly illustrates the overall decrease in G with depth for flash heating, over the whole computed range of total slip, together with the increase in G with depth for thermal pressurization. In addition to this general trend, some complexity appears at shallow depth, where the mechanism associated with the lowest fracture energy switches from flash heating at small slip to thermal pressurization at large slip. This highlights the limitation of our approach, which analyzes the two mechanisms separately, and clearly demonstrates the need for a coupled approach. An additional natural step is to also include realistic slip rate histories during rupture, as done for instance in Viesca and Garagash [2015].

Velocity-weakening mechanisms like flash heating tend to produce different rupture styles than slip-weakening mechanisms, with a propensity to develop self-healing as opposed to crack-like ruptures [e.g., Cochard and Madariaga, 1994; Zheng and Rice, 1998]. As demonstrated by Zheng and Rice [1998], in velocity-weakening faults there exists a critical background shear stress, denoted τ_{pulse} , below which no crack-like ruptures can

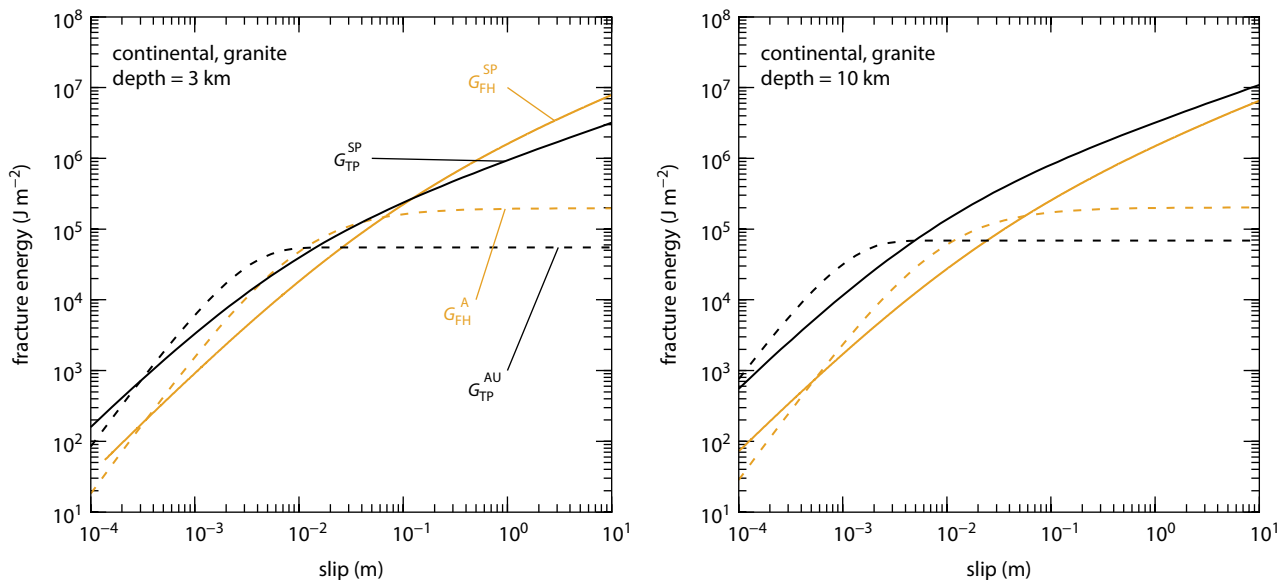


Figure 9.10 Estimates of fracture energy for both thermal pressurization and flash heating, as a function of slip, illustrated in the case of the continental crust at 3 km (left) and 10 km (right) depth. For the adiabatic (undrained) limits, a shear zone width of $W = 100 \mu\text{m}$ is chosen. In all cases a constant slip rate of $V = 1 \text{ ms}^{-1}$ is imposed. See electronic version for color representation.

propagate and the only possible rupture mode is a self-healing slip pulse. For stresses significantly below the threshold τ_{pulse} , propagating ruptures tend to behave as decaying slip pulses and naturally stop, while at larger stresses ruptures are expanding slip pulses and beyond τ_{pulse} they become crack-like. Therefore, τ_{pulse} is an instructive measure of the possible rupture styles and of the threshold stress below which ruptures will naturally arrest.

Following *Zheng and Rice* [1998], τ_{pulse} is defined as the maximum background stress τ_b satisfying $\tau_b - (\mu/2c_s)V \leq \tau(V)$, where μ is the shear modulus of the material hosting the rupture, c_s is its shear wave speed, V is the slip rate, and $\tau(V)$ is the dynamic strength. In the case of flash heating, assuming constant $V_{w,\text{gouge}}$ (or V_w when modeling friction between bare rock surfaces), τ_{pulse} can be computed using equation (9.7) as

$$\tau_{\text{pulse}} = \sqrt{2\mu f_0(\sigma_n - p_0)V_{w,\text{gouge}}/c_s}, \quad (9.44)$$

where we have neglected the contribution of f_w . Profiles of τ_{pulse} as a function of depth are shown in Figure 9.11, where the static ‘‘Byerlee’’ frictional strength $f_0(\sigma_n - p_0)$ is also plotted for comparison. The threshold τ_{pulse} is typically of the order of a few tens of MPa throughout the depths investigated. By contrast, the static frictional strength increases linearly with depth according to the effective pressure gradient. In our computation for a continental crust using quartz properties (Figure 9.11a), τ_{pulse} remains nearly constant at around 10 to 20 MPa, much smaller than the static strength, which implies that crack-like dynamic ruptures can easily propagate at stresses much below the local ‘‘Byerlee’’ strength. In our modeled oceanic setting (Figure 9.11b), τ_{pulse} is initially larger than the static strength, down to a depth of around 3 km. Therefore, the shallow part of faults hosted in the oceanic crust is expected to only rupture in the self-healing pulse mode (or not rupture dynamically at all unless other weakening mechanisms are active). In the subduction setting with hydrostatic pore pressure gradient (Figure 9.11c, solid lines), τ_{pulse} remains significantly smaller than $f_0(\sigma_n - p_0)$ across most of the profile, reproducing a similar situation as in the continental crust. However, for near-lithostatic pore pressure profiles, the static strength is lower than τ_{pulse} down to around 30 km depth, which implies that the top part of subduction zones are unlikely to generate crack-like ruptures if friction is controlled by flash heating in gouge.

Because other weakening mechanisms, such as thermal pressurization, are involved during earthquake propagation, the stress level τ_{pulse} computed here based on flash heating only can be viewed as an upper bound of the actual stress separating pulse from cracks [*Noda et al.*, 2009]. Furthermore, our expression for τ_{pulse} (equation [9.44]) is based on the assumption that the weakening velocity V_w is constant, i.e., neglecting the complex thermal effects out-

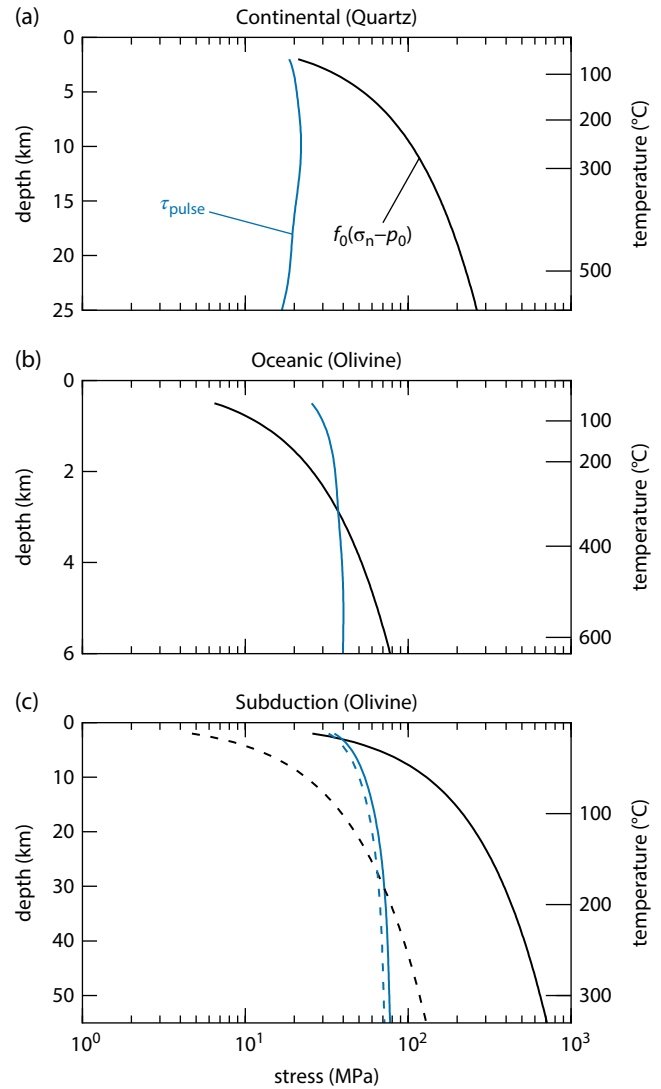


Figure 9.11 Profiles of τ_{pulse} (blue) and peak (static) frictional strength $f_0(\sigma_n - p_0)$ (black) as a function of depth, in continental (a), oceanic (b) and subduction (c) settings. Solid lines correspond to hydrostatic pore pressure gradients, and dashed lines (in subplot [c]) correspond to sublithostatic pore pressure gradients. The threshold τ_{pulse} separates a low-stress regime, in which only self-healing ruptures can propagate, and a high-stress regime, in which crack-like ruptures dominate. See *electronic version for color representation*.

lined in section 9.2. Hence, equation (9.44) is valid for flash heating provided that the bulk temperature rise (and thus slip) is small. For large slips leading to a significant temperature rise, the weakening velocity decreases and our value of τ_{pulse} again provides an upper bound. Note, however, that the details of the rupture style (pulse vs. crack) in complex ruptures scenarios involving flash heating with thermal effects and thermal pressurization require fully dynamic rupture simulations, and predictions of rupture style based on a simple stress threshold might be very crude.

9.5. DISCUSSION

Our analysis demonstrates that thermal pressurization tends to be most efficient at midcrustal depths owing to the changes in the properties of water, while flash heating becomes more efficient with increasing depth due to the gradual reduction in the difference between ambient and weakening temperatures. The efficiency of flash heating is encapsulated by a combination of a critical slip rate $V_{w, \text{gouge}}$ and critical times t_w^A and t_w^{SP} , while thermal pressurization is controlled by a critical strain γ_c at early times (independent from the slip rate) and a critical slip L^* (slip rate dependent) at larger slips. In this section, we discuss (i) limitations associated with the modeling approach, (ii) other potential weakening mechanisms that could be activated during seismic slip, and finally (iii) the implications of our results for the propagation of earthquakes down to the base of the seismogenic zone.

9.5.1. Limitations of the Approach

For simplicity we assumed a constant slip rate $V = 1 \text{ ms}^{-1}$, though we highlighted how our analysis would depend on the exact slip rate history of the fault. Here we reiterate the subtle differences between the slip rate dependence of flash heating and thermal pressurization. For flash heating, it follows from our assumption of $f_w = 0$ that the temperature evolution, and thus the evolution of the weakening velocity, is independent of the slip rate history. The use of $f_w = 0$, although apparently arbitrary, appears to be quite natural in the absence of direct experimental measurements, and also considering that the strength of weakened asperities is unlikely to be simply frictional. Above the weakening velocity, the shear strength is controlled by the ratio of the weakening velocity to the slip rate, so the shear strength evolution is highly sensitive to the slip rate history. However, because the friction coefficient is proportional to $1/V$, the fracture energy is equal to the integral of the weakening velocity with respect to time. Thus, while the shear strength evolution for flash heating is sensitive to the slip rate history, the fracture energy is totally independent of the slip rate history of the fault and depends only on the slip duration. Obviously for slip rates below the weakening velocity, there is no dependence of shear strength on slip rate, though flash heating is likely triggered at larger slips if significant heat is produced during seismic slip because the weakening velocity depends strongly on the fault temperature.

In contrast with flash heating, the dependence on slip rate varies between the two limits for thermal pressurization. For deformation under undrained and adiabatic conditions, the shear strength evolution is insensitive to the details of the slip rate evolution and depends only on the total strain (i.e. slip) accommodated by the gouge

layer. This naturally leads to a fracture energy that is also independent of slip rate. Because thermal pressurization depends not only on generating high pore pressures but also on confining high pore pressures through inefficient hydrothermal diffusion into the surrounding material, the slip-on-a-plane limit is sensitive to the slip rate history. This can be clearly seen in the analytic solution for a constant slip rate, where the critical weakening slip L^* scales with $1/V$. In general, lowering the slip rate allows more efficient diffusion to occur for a given slip, and thus a higher shear strength and fracture energy. No analytic solutions exist for a variable slip rate, but the balance between the rates at which frictional heating generates pore pressures and hydrothermal diffusion relieves elevated pore pressures can be clearly seen in the solutions of *Garagash* [2012] for steady slip pulses driven by thermal pressurization. If the slip rate drops near the trailing edge of a rupture, then hydrothermal diffusion can dominate frictional heating, leading to rapid restrengthening. Of the four weakening scenarios considered in this chapter, thermal pressurization in the slip-on-a-plane limit displays the most varied range of behavior as the slip rate history changes.

Another major limitation of our model is the assumption of a constant shear zone width W . Flash heating and thermal pressurization both drive strain localization, so W is unlikely to remain constant during an earthquake [see *Rice et al.*, 2014; *Platt et al.*, 2014b, 2015]. Localization leads to more efficient weakening for both mechanisms. However, *Platt et al.* [2014b] showed that for thermal pressurization the onset of localization leads to a transition from the undrained and adiabatic limit to the slip-on-a-plane limit. Thus, our analysis with constant W likely still captures the essential elements of weakening. A detailed assessment of the effect of changes in W during rupture remains only accessible through detailed numerical computations.

Despite the important caveats regarding the evolution of slip rate and deforming zone thickness, our approach remains robust in terms of predicting the *relative* efficiency of flash heating and thermal pressurization with depth because the physics of these processes does not change. Flash heating will still become more efficient with depth as the background temperature approaches the weakening temperature, and the efficiency of thermal pressurization will be largely controlled by Λ and α_{hy} .

Finally, we have neglected to model additional physics that may become important near the onset of bulk melting of the fault rock. Flash heating induces a weakening because the load-bearing asperities breakdown at high temperatures. However, when the background temperature reaches the melting point, the concept of load-bearing asperities is no longer valid, and the rock might even transiently strengthen at the onset of melting. Such transient restrengthening has been observed experimentally

[e.g., *Hirose and Shimamoto*, 2005]. In addition, if the melting temperature increases with pressure, then bulk melting may occur at temperatures below the asperity-scale melting temperature. No models currently exist for the transition from asperity-scale to bulk weakening, limiting our ability to properly quantify these processes.

9.5.2. Other Weakening/Strengthening Mechanisms

In this chapter we focus on flash heating and thermal pressurization, two well-studied processes thought to start immediately at the onset of sliding with strong quantitative support from high-velocity friction experiments [*Goldsby and Tullis*, 2011; *Goldsby et al.*, 2014; *Proctor et al.*, 2014]. However, a number of other weakening mechanisms have been proposed [see *Niemeijer et al.*, 2012]. Two efficient weakening mechanisms operating at relatively large slip are frictional melting [e.g., *Hirose and Shimamoto*, 2005; *Nielsen et al.*, 2008] and thermo-chemical pressurization [*Sulem and Famin*, 2009; *Brantut et al.*, 2010].

While the onset of melting may lead to transient restrengthening, melting leads to significant weakening once a continuous melt layer forms. The exact weakening depends on the melt viscosity, and thus the mineralogy of the fault, and the temperature dependence of the viscosity naturally leads to strain localization within the melt layer [*Nielsen et al.*, 2008, 2010].

Thermo-chemical pressurization corresponds to the release of fluids from devolatilization reactions such as decarbonation of carbonates [e.g., *Han et al.*, 2007] or dehydroxylation of clays [e.g., *Brantut et al.*, 2008]. Under typical crustal conditions, devolatilization reactions have a positive total volume change, and thus the released fluids are pressurized and further weaken the fault. Thermo-chemical pressurization is inherently linked to the presence of specific minerals (e.g., carbonates or clays) and is activated near threshold temperatures that correspond to each specific reaction, though the rate of weakening is typically dictated by the reaction kinetics.

Because both frictional heating and thermo-chemical pressurization are triggered once the fault temperature reaches a critical value, neither mechanism is expected to be active at the onset of slip and, depending on the efficiency of weakening provided by thermal pressurization, may never be triggered. The presence of a critical temperature means that both mechanisms are expected to provide relatively discrete weakening, in contrast with the more continuous weakening provided by flash heating and thermal pressurization.

Due to the sensitive dependence on the fault mineralogy and the uncertainty in peak temperature, we did not attempt to model thermo-chemical pressurization and frictional melting. In particular, addressing all of the possible variations in mineralogy far exceeds the scope of

this chapter. The reluctance to address a wide range of mineralogy is partly responsible for our assumption of a constant weakening temperature in our flash heating model (which could range between a few hundred degrees C for thermally unstable clays, up to more than 2000°C for the hardest oxides), though the poor constraints on the exact asperity-scale mechanisms that lead to weakening also played a role.

Despite not quantifying the weakening due to frictional melting and thermo-chemical pressurization, we speculate on the role they could play during dynamic rupture. Both mechanisms are most likely to be triggered near the base of the seismogenic zone where the temperature rises are largest. However, *Platt et al.* [2015] showed that thermo-chemical pressurization is controlled by the ratio of total pore pressure generated by the reaction and the ambient effective stress, so if the reaction-induced excess pressure is roughly constant with depth, then thermo-chemical pressurization will become less efficient with depth, at least if the effective normal stress increases with depth. In contrast, we expect frictional melting to become more efficient with depth because the dissipation rate increases, and thus a thicker melt layer can be formed. Conversely, while both mechanisms are likely rarely active at shallow depths, if triggered they could provide dramatic weakening.

Throughout this chapter we have considered only shear weakening mechanisms, but strength is not necessarily a decreasing function of slip. In particular, if dilatancy occurs, pore pressure can potentially decrease at the onset of slip, producing an initial strengthening accompanied by an excess heat production. A simple way to consider this problem, given by *Rice* [2006], is to assume that dilatancy occurs nearly instantaneously and has the effect of resetting the initial pore pressure. In the most extreme scenario, such as during the rupture of an intact rock, dilatancy could generate enough voids to desaturate the rock; in that case, only flash heating and potentially frictional melting could be considered as weakening mechanisms. In less extreme situations, *Garagash and Rudnicki* [2003] showed that strengthening by dilatancy can quickly be compensated for by thermal pressurization due to the excess heat generated; however, this excess heat could lead to premature melting. While the effect of dilatancy could potentially be dramatic, in the absence of a consistent published data set on dilatancy in overconsolidated materials during high-speed friction, modelling of such processes remains somewhat premature.

9.5.3. Implications for Earthquake Propagation at the Base of Seismogenic Zone

Our computations provide first-order estimates of the efficiency of thermal pressurization and flash heating mechanisms as a function of depth. For thermal pressurization, in

both our continental and oceanic crust models we observe a trend toward lower efficiency below midcrustal depths (around 10 km and 3 km depth for the continental and oceanic crust, respectively), which correspond approximately to the brittle-plastic transition in each case [e.g., *Kohlstedt et al.*, 1995]. Nevertheless, the decrease in efficiency (as illustrated, for instance, by the increase in fracture energy in Figure 9.8) below these depths is not strongly marked, and it is difficult to make the case for a threshold that would delineate the base of the seismogenic zone. Flash heating becomes generally increasingly efficient with increasing depth (see Figure 9.9), and again, no clear change exists that could set the base of the seismogenic zone. Therefore, constitutive dynamic rheology alone is insufficient to set the ultimate propagation depth of earthquakes.

In order to explain why earthquakes do not propagate through the whole lithosphere, we must appeal to additional mechanisms. One major process occurring at depth in the crust is creep of rocks, aided by the presence of water, which has two main effects: (i) it tends to heal and seal fault rocks, generating low-porosity cataclasites (typically below the 150°C isotherm [*Sibson*, 1986]) as opposed to the granulated, incohesive fault gouge that remains at shallow depths; (ii) it relaxes the long-term shear stress applied on faults.

The effect of healing and sealing of porosity is potentially dramatic for thermal pressurization, because it implies that earthquake slip is initially accompanied by dilatancy, which decreases the initial pore pressure [*Rice*, 2006] and makes thermal pressurization much less effective. In addition, porosity healing and sealing could also reduce the effective pressure coefficient [*Hirth and Beeler*, 2015], which both reduces the rapidity of thermal pressurization and prevents a total strength drop.

The stress relaxation due to creep tends to smooth stress heterogeneities and to lower the background shear stress. With increasing depth, creep relaxation becomes more efficient and the driving stresses decrease, implying that earthquake ruptures propagating downward would enter into regions of decreased background stress and naturally stop. This is illustrated in Figure 9.12, which shows upper limits on fault strength based on static friction (using $f_0 = 0.6$) and creep flow laws for both our modeled continental and oceanic settings, as well as values of τ_{pulse} . In the continental crust, below 15 km depth, τ_{pulse} (for gouge) becomes larger than the creep strength, which implies that crack-like ruptures driven by flash heating cannot propagate, and that self-healing ruptures propagating downward will decay. For bare rock surfaces, the transition is at around 22 km depth.

To illustrate how the creep strength would compare with dynamically weakened friction, we also plot in Figure 9.12 tentative frictional strength using arbitrarily low friction

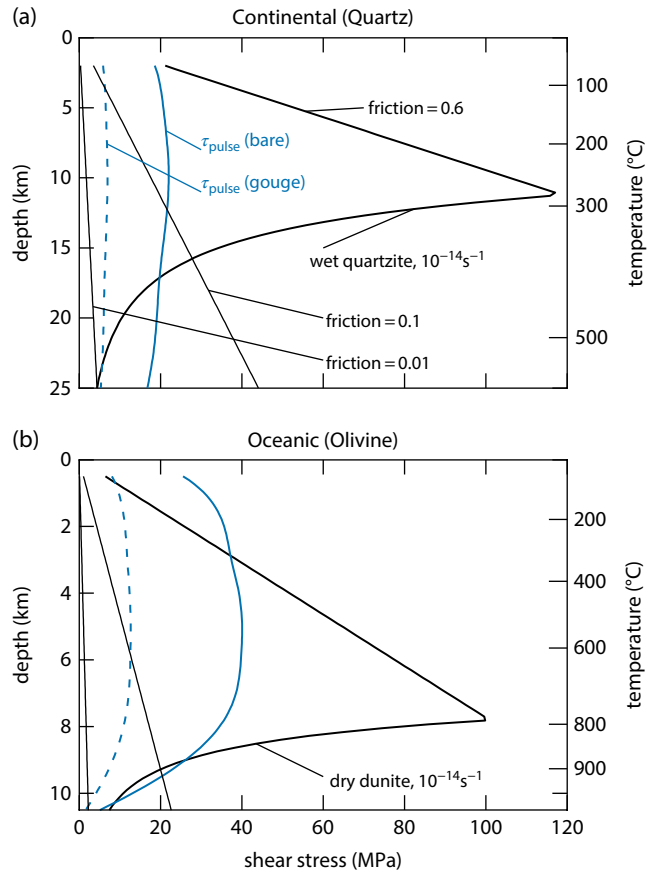


Figure 9.12 Critical stress and strength levels in the continental (a) and oceanic (b) lithosphere. Thick black lines correspond to the upper limit for strength based on Byerlee's rule and flow law for wet quartzite [*Hirth et al.*, 2001] and dry dunite [*Hirth and Kohlstedt*, 2003] at 10^{-14} s^{-1} strain rate. Flow laws provide limits for differential stress, which was converted to resolved shear stress assuming that the fault is optimally oriented for frictional slip. Thin black lines are frictional strength assuming friction coefficients of 0.1 and 0.01, shown as potential lower limits for dynamic strength due to flash heating. Blue curves correspond to τ_{pulse} as computed for gouge (solid lines) or bare rock surfaces (dashed lines). See electronic version for color representation.

coefficients of 0.1 and 0.01 (which are used as representative estimates of the minimum friction level achieved during flash heating). Using a frictional strength with a friction coefficient of 0.1 to mimic the dynamic strength due to flash heating, we find that the creep strength, and therefore the maximum background shear stress on the fault, becomes lower than the dynamic strength below 15 km. For an even lower friction coefficient of 0.01, that crossover depth is 22 km. Because the creep strength decreases dramatically with increasing temperature, the crossover depth is only modestly sensitive to the specific value of the friction coefficient, which moderates the impact of having to choose arbitrary values. Below the

crossover depth, the potential stress drop decreases dramatically and dynamic ruptures will tend to stop. Taken together, these observations suggest that the maximum depth for earthquake propagation (driven by flash heating) is between 15 and 22 km. A similar construction is done for the oceanic lithosphere (Figure 9.12b), for which we find that the transition depth, both in terms of τ_{pulse} and dynamic friction, is around 8 km. The temperature profile in our model is such that the 1000°C isotherm is crossed at around 11 km depth. Because we assumed $T_w = 1000^\circ\text{C}$ in our flash heating calculations, weakening by flash heating below the 1000°C isotherm is not meaningful and the physics of high-velocity friction might be different (see section 9.5.1).

Overall, our calculations show that dynamic ruptures are efficiently stopped at depth due to a decrease in background stress, capped by the long-term creep strength of the fault rocks. Interestingly, we also note that rupture *can* propagate across the brittle-plastic transition, in regions where the upper limit given by friction or plastic flow is significantly higher than the dynamic strength, because of the high efficiency of dynamic weakening mechanisms, such as flash heating, at great depth. This is consistent with the fault zone model of *Scholz* [1988] and with the existence of fault rocks that exhibit mixtures of seismic (e.g., pseudotachylytes) and creep (e.g., mylonites) features [e.g., *Sibson*, 1980].

In the case of subduction zones, the brittle-to-plastic transition occurs at greater depths than those of interest here. Hence, our results do not indicate any marked threshold for the maximum propagation depth. This is consistent with the continuous seismicity observed along subducting slabs. However, our results here are likely oversimplified because we did not account for the presence of weak minerals, like serpentines, that can produce low-stress zones [e.g., *Hilairet et al.*, 2007] and naturally prevent dynamic ruptures from propagating downward. Furthermore, prograde metamorphic reactions are also expected to generate complex lithological and stress/strength patterns, which is not captured by our simple approach. It is clear that the subduction zones should receive improved attention and refined modeling approaches to unravel their complexity and the associated seismic risk.

9.6. CONCLUSIONS

We have computed a series of characteristic parameters that describe how two major dynamic weakening mechanisms, thermal pressurization and flash heating, operate in a set of representative geological settings. Flash heating is initially controlled by a critical slip rate, but further weakening is induced by gradual increases in temperature due to shear heating. These thermal effects are controlled by critical times t_w^A (for adiabatic conditions, at small slip)

and t_w^{SP} (for slip-on-a-plane conditions, at large slip). The original formulation of flash heating was designed for bare rock surfaces; in gouge, flash heating is much less efficient (i.e., occurs at higher slip rates) and thermal effects likely dominate the weakening. Thermal pressurization is primarily controlled by the so-called thermal pressurization factor Λ , which quantifies the pore fluid pressure increase produced by a unit increase in fault zone temperature under undrained conditions, and strongly depends on the compressibility and thermal expansivity of the fluid. At small slip (under undrained, adiabatic conditions), the weakening due to thermal pressurization is controlled by a critical strain γ_c , while it is controlled by a critical slip L^* at large slip (in the slip-on-a-plane limit).

In all our computations, the critical weakening times t_w^A and t_w^{SP} , as well as the nominal critical weakening velocity V_w^* , tend to decrease with increasing depth, making flash heating the most efficient weakening mechanism near the base of the seismogenic zone. Due to the change in compressibility and thermal expansivity of water with increasing pressure and temperature at depth, the thermal pressurization factor Λ tends to peak at midcrustal depths (around 10 km and 3 km in the continental and oceanic crust, respectively), therefore making thermal pressurization the most efficient at these depths.

The maximum propagation depth of earthquake ruptures in both the continental and oceanic lithosphere is likely located significantly below the brittle-plastic transition and is mainly controlled by the lack of sufficient driving shear stresses due to efficient creep processes.

ACKNOWLEDGMENTS

This work was supported by the UK Natural Environment Research Council through grant NE/K009656/1 to N.B. and by a Post-Doctoral Fellowship of the Carnegie Institution to J.D.P. The authors thank Jim Rice and Rob Viesca for fruitful discussions. Comments by two anonymous reviewers helped to clarify the manuscript. The Matlab codes used to generate the results of this paper are available at https://github.com/nbrantut/Dynamic_Weakening_Depth.

REFERENCES

- Ampuero, J.-P., and A. M. Rubin (2008), Earthquake nucleation on rate and state faults: Aging and slip laws, *J. Geophys. Res.*, *113*, B01302, doi:10.1029/2007JB005082.
- Andrews, D. J. (2002), A fault constitutive relation accounting for thermal pressurization of pore fluid, *J. Geophys. Res.*, *107*(B12), 2363, doi:10.1029/2002JB001942.
- Archard, J. F. (1958/1959), The temperature of rubbing surfaces, *Wear*, *2*, 438–455.

- Beeler, N. M., T. E. Tullis, and D. L. Goldsby (2008), Constitutive relationships and physical basis of fault strength due to flash heating, *J. Geophys. Res.*, *113*, B01401, doi:10.1029/2007JB004988.
- Boettcher, M. S., G. Hirth, and B. Evans (2007), Olivine friction at the base of oceanic seismogenic zones, *J. Geophys. Res.*, *112*, B01205, doi:10.1029/2006JB004301.
- Brace, W. F., and D. L. Kohlstedt (1980), Limits on lithospheric stress imposed by laboratory experiments, *J. Geophys. Res.*, *85*(B11), 6248–6252.
- Brantut, N., R. Han, T. Shimamoto, N. Findling, and A. Schubnel (2011), Fast slip with inhibited temperature rise due to mineral dehydration: Evidence from experiments on gypsum, *Geology*, *39*(1), 59–62.
- Brantut, N., A. Schubnel, J. Corvisier, and J. Sarout (2010), Thermochemical pressurization of faults during coseismic slip, *J. Geophys. Res.*, *115*, B05314, doi:10.1029/2009JB006533.
- Brantut, N., A. Schubnel, J.-N. Rouzaud, F. Brunet, and T. Shimamoto (2008), High velocity frictional properties of a clay-bearing fault gouge and implications for earthquake mechanics, *J. Geophys. Res.*, *113*, B10401, doi:10.1029/2007JB005551.
- Brune, J. N. (1970), Tectonic stress and the spectra of seismic shear waves from earthquakes, *J. Geophys. Res.*, *75*(26), 4997–5009.
- Carslaw, H. S., and J. C. Jaeger (1959), *Conduction of heat in solids*, 2nd ed., Oxford University Press, New York.
- Chapman, D. S. (1986), Thermal gradients in the continental crust, in *The nature of the lower continental crust*, *Special Publications*, vol. 24, edited by J. B. Dawson, D. A. Carswell, J. Hall, and K. H. Wedepohl, pp. 63–70, Geological Society, London.
- Chen, J., and A. W. Rempel (2014), Progressive flash heating and the evolution of high-velocity rock friction, *J. Geophys. Res.*, *119*(4), 3182–3200, doi:10.1002/2013JB010631.
- Clauser, C., and E. Huenges (1995), Thermal conductivity of rocks and minerals, in *Rock physics and phase relations: A handbook of physical constants*, edited by T. J. Ahrens, AGU Reference Shelf, American Geophysical Union, Washington, DC.
- Cochard, A., and R. Madariaga (1994), Dynamic faulting under rate-dependent friction, *Pure Appl. Geophys.*, *142*(3/4), 419–445.
- Di Toro, G., D. Goldsby, and T. E. Tullis (2004), Friction falls towards zero in quartz rock as slip velocity approaches seismic rates, *Nature*, *427*, 436–439.
- Di Toro, G., R. Han, T. Hirose, N. De Paola, S. N. K. Mizoguchi, F. Ferri, M. Cocco, and T. Shimamoto (2011), Fault lubrication during earthquakes, *Nature*, *471*, 494–498.
- Di Toro, G., G. Pennacchioni, and G. Teza (2005), Can pseudotachylites be used to infer earthquake source parameters? An example of limitations in the study of exhumed faults, *Tectonophysics*, *402*, 3–20.
- Dieterich, J. H. (1978), Time-dependent friction and mechanics of stick-slip, *Pure Appl. Geophys.*, *116*, 790–806.
- Evans, B. (1984), The effect of temperature and impurity content on indentation hardness of quartz, *J. Geophys. Res.*, *89*(B6), 4213–4222.
- Evans, B., and C. Goetze (1979), The temperature variation of hardness of olivine and its implication for polycrystalline yield stress, *J. Geophys. Res.*, *84*(B10), 5505–5524.
- Garagash, D. I. (2012), Seismic and aseismic slip pulses driven by thermal pressurization of pore fluid, *J. Geophys. Res.*, *117*, B04314, doi:10.1029/2011JB008889.
- Garagash, D. I., and J. W. Rudnicki (2003), Shear heating of a fluid-saturated slip-weakening dilatant fault zone: 1. Limiting regimes, *J. Geophys. Res.*, *108*(B2), 2121, doi:10.1029/2001JB001653.
- Goldsby, D. L., and T. E. Tullis (2002), Low frictional strength of quartz rocks at subseismic slip rates, *Geophys. Res. Lett.*, *29*(17), 1844, doi:10.1029/2002GL015240.
- Goldsby, D. L., and T. E. Tullis (2011), Flash heating leads to low frictional strength of crustal rocks at earthquake slip rates, *Science*, *334*, 216–218.
- Goldsby, D. L., T. E. Tullis, K. Okazaki, J. D. Platt, and T. M. Mitchell (2014), Experimental studies of dynamic fault weakening due to thermal pore-fluid pressurization, abstract S11C-4357 presented at 2014 Fall Meeting, AGU, San Francisco, Calif., 15–19 December.
- Hacker, B. R., G. A. Abers, and S. M. Peacock (2003), Subduction factory: 1. Theoretical mineralogy, densities, seismic wave speeds, and H₂O content, *J. Geophys. Res.*, *108*(B1), 2029, doi:10.1029/2001JB001127.
- Han, R., T. Shimamoto, T. Hirose, J. Ree, and J. Ando (2007), Ultra-low friction of carbonate faults caused by thermal decomposition, *Science*, *316* (5826), 878–881.
- Hilaret, N., B. Reynard, Y. Wang, I. Daniel, S. Merkel, N. Nishiyama, and S. Petitgirard (2007), High-pressure creep of serpentine, interseismic deformation, and initiation of subduction, *Science*, *318* (5858), 1910–1913.
- Hirose, T., and M. Bystricky (2007), Extreme dynamic weakening of faults during dehydration by coseismic shear heating, *Geophys. Res. Lett.*, *34*, L14311, doi:10.1029/2007GL030049.
- Hirose, T., and T. Shimamoto (2005), Growth of molten zone as a mechanism of slip weakening of simulated faults in gabbro during frictional melting, *J. Geophys. Res.*, *110*, B05202, doi:10.1029/2004JB003207.
- Hirth, G., and N. M. Beeler (2015), The role of fluid pressure on friction behavior at the base of the seismogenic zone, *Geology*, *43* (3), 223–226.
- Hirth, G., and D. L. Kohlstedt (2003), Rheology of the upper mantle and the mantle wedge: A view from the experimentalists, in *Inside the subduction factory*, *Geophys. Monogr. Ser.*, vol. 138, edited by J. Eiler, pp. 83–105, American Geophysical Union, Washington, DC.
- Hirth, G., C. Teyssier, and W. J. Dunlap (2001), An evaluation of quartzite flow laws based on comparisons between experimentally and naturally deformed rocks, *Geol. Rundsch.*, *90*, 77–87.
- Jaupart, C., and J.-C. Mareschal (2007), Heat flow and thermal structure of the lithosphere, in *Treatise on Geophysics*, vol. 6, edited by G. Schubert, pp. 217–251, Elsevier, Oxford.
- Junglas, P. (2009), WATER95—A MATLAB implementation of the IAPWS-95 standard for use in thermodynamics lectures, *Int. J. Engng. Ed.*, *25*(1), 3–18.

- Kohlstedt, D. L., B. Evans, and S. J. Mackwell (1995), Strength of the lithosphere: Constraints imposed by laboratory experiments, *J. Geophys. Res.*, *100*(B9), 17,587–17,602.
- Lachenbruch, A. H. (1980), Frictional heating, fluid pressure, and the resistance to fault motion, *J. Geophys. Res.*, *85*, 6097–6122.
- Lachenbruch, A. H., and J. H. Sass (1980), Heat flow and energetics of the San Andreas fault zone, *J. Geophys. Res.*, *85*(B11), 6185–6223.
- Lapusta, N., and J. R. Rice (2003), Low-heat and low-stress fault operation in earthquake models of statically strong but dynamically weak faults, *Eos. Trans. AGU*, *84*(46), Fall Meet. Suppl., Abstract S51B-02.
- Marone, C., and C. H. Scholz (1988), The depth of seismic faulting and the upper transition from stable to unstable slip regimes, *Geophys. Res. Lett.*, *15*(6), 621–624.
- Mase, C. W., and L. Smith (1985), Pore-fluid pressures and frictional heating on a fault surface, *Pure Appl. Geophys.*, *122*, 583–607.
- Mase, C. W., and L. Smith (1987), Effects of frictional heating on the thermal, hydrologic, and mechanical response of a fault, *J. Geophys. Res.*, *92* (B7), 6249–6272.
- McKenzie, D., J. Jackson, and K. Priestley (2005), Thermal structure of oceanic and continental lithosphere, *Earth Planet. Sci. Lett.*, *233*, 337–349.
- Nielsen, S., G. Di Toro, T. Hirose, and T. Shimamoto (2008), Frictional melt and seismic slip, *J. Geophys. Res.*, *113*, B01308, doi:10.1029/2007JB005122.
- Nielsen, S., P. Mosca, G. Giberti, G. Di Toro, T. Hirose, and T. Shimamoto (2010), On the transient behavior of frictional melt during seismic slip, *J. Geophys. Res.*, *115*, B10301, doi:10.1029/2009JB007020.
- Niemeijer, A., G. Di Toro, W. A. Griffith, A. Bistacchi, S. A. F. Smith, and S. Nielsen (2012), Inferring earthquake physics and chemistry using an integrated field and laboratory approach, *J. Struct. Geol.*, *39*, 2–36.
- Noda, H., E. M. Dunham, and J. R. Rice (2009), Earthquake ruptures with thermal weakening and the operation of major faults at low overall stress levels, *J. Geophys. Res.*, *114*, B07302, doi:10.1029/2008JB006143.
- Noda, H., and T. Shimamoto (2005), Thermal pressurization and slip-weakening distance of a fault: An example of Hanaore fault, southwest Japan, *Bull. Seism. Soc. Am.*, *95*(4), 1224–1233.
- Palmer, A. C., and J. R. Rice (1973), The growth of slip surfaces in the progressive failure of over-consolidated clay, *Proc. Roy. Soc. Lond. A.*, *332*, 527–548.
- Parsons, B., and J. G. Sclater (1977), An analysis of the variation of ocean floor bathymetry and heat flow with age, *J. Geophys. Res.*, *82* (5), 803–827.
- Passelègue, F. X., D. L. Goldsby, and O. Fabbri (2014), The influence of ambient fault temperature on flash-heating phenomena, *Geophys. Res. Lett.*, *41*, doi:10.1002/2013GL058374.
- Peacock, S. M., N. I. Christensen, M. G. Bostock, and P. Audet (2011), High pore pressures and porosity at 35 km depth in the Cascadia subduction zone, *Geology*, *39*(5), 471–474, doi:10.1130/G31649.1.
- Platt, J. D., N. Brantut, and J. R. Rice (2015), Strain localization driven by thermal decomposition during seismic shear, *J. Geophys. Res.*, *120*, doi:10.1002/2014JB011493.
- Platt, J. D., B. Proctor, T. M. Mitchell, G. Hirth, D. L. Goldsby, G. Di Toro, N. M. Beeler, and T. E. Tullis (2014a), The role of gouge and temperature on flash heating and its hysteresis, abstract S11C-4360 presented at 2014 Fall Meeting, AGU, San Francisco, Calif., 15–19 December.
- Platt, J. D., J. W. Rudnicki, and J. R. Rice (2014b), Stability and localization of rapid shear in fluid-saturated fault gouge: 2. Localized zone width and strength evolution, *J. Geophys. Res.*, *119*, 4334–4359, doi:10.1002/2013JB010711.
- Proctor, B. P., T. M. Mitchell, G. Hirth, D. Goldsby, F. Zorzi, J. D. Platt, and G. Di Toro (2014), Dynamic weakening of serpentinite gouge and bare-surfaces at seismic slip rates, *J. Geophys. Res.*, *119*, doi:10.1002/2014JB011057.
- Rempel, A., and J. R. Rice (2006), Thermal pressurization and onset of melting in fault zones, *J. Geophys. Res.*, *111*, B09314, doi:10.1029/2005JB004006.
- Rempel, A. W. (2006), The effects of flash-weakening and damage on the evolution of fault strength and temperature, in *Earthquakes: Radiated energy and the physics of faulting*, *Geophys. Monogr. Ser.*, vol. 170, edited by R. Abercrombie, A. McGarr, G. Di Toro, and H. Kanamori, pp. 263–270, American Geophysical Union, Washington, DC.
- Rempel, A. W., and S. L. Weaver (2008), A model for flash weakening by asperity melting during high-speed earthquake slip, *J. Geophys. Res.*, *113*, B11308, doi:10.1029/2008JB005649.
- Rice, J. R. (1996), Low-stress faulting: Strong but brittle faults with local stress concentrations, *Eos. Trans. AGU*, *77*(46), Fall Meet. Suppl., F6811.
- Rice, J. R. (1999), Flash heating at asperity contacts and rate-depend friction, *Eos. Trans. AGU*, *80*(46), Fall Meet. Suppl., F6811.
- Rice, J. R. (2006), Heating and weakening of faults during earthquake slip, *J. Geophys. Res.*, *111*, B05311, doi:10.1029/2005JB004006.
- Rice, J. R., N. Lapusta, and K. Ranjith (2001), Rate and state dependent friction and the stability of sliding between elastically deformable solids, *J. Mech. Phys. Solids*, *49*, 1865–1898.
- Rice, J. R., J. W. Rudnicki, and J. D. Platt (2014), Stability and localization of rapid shear in fluid-saturated fault gouge: 1. Linearized stability analysis, *J. Geophys. Res.*, *119*, 4311–4333, doi:10.1002/2013JB010711.
- Rice, J. R., and A. L. Ruina (1983), Stability of steady frictional slipping, *J. Appl. Mech.*, *105*, 343–349.
- Rubin, A. M., and J.-P. Ampuero (2005), Earthquake nucleation on (aging) rate and state faults, *J. Geophys. Res.*, *110*, B11312, doi:10.1029/2005JB003686.
- Ruina, A. L. (1983), Slip instability and state variable friction laws, *J. Geophys. Res.*, *88*, 10,359–10,370.
- Scholz, C. H. (1988), The critical slip distance for seismic faulting, *Nature*, *336*, 761–763.
- Scholz, C. H. (1998), Earthquakes and friction laws, *Nature*, *391*, 37–42.
- Scholz, C. H. (2002), *The mechanics of earthquake and faulting*, 2nd ed., Cambridge University Press, Cambridge, United Kingdom.
- Sibson, R. H. (1980), Transient discontinuities in ductile shear zones, *J. Struct. Geol.*, *2*, 165–171.

- Sibson, R. H. (1986), Earthquakes and rock deformation in crustal fault zones, *Ann. Rev. Earth Planet. Sci.*, *14*, 149–75.
- Sulem, J., and V. Famin (2009), Thermal decomposition of carbonates in fault zones: slip-weakening and temperature-limiting effects, *J. Geophys. Res.*, *114*, B03309, doi:10.1029/2008JB005912.
- Turcotte, D. L., and G. Schubert (2002), *Geodynamics*, 2nd ed., Cambridge University Press, New York.
- Viesca, R. C., and D. I. Garagash (2015), Ubiquitous weakening of faults due to thermal pressurization, *Nat. Geosci.*, doi:10.1038/ngeo2554.
- Vosteen, H.-D., and R. Schellschmidt (2003), Influence of temperature on thermal conductivity, thermal capacity and thermal diffusivity for different types of rock, *Phys. Chem. Earth*, *28*, 499–509.
- Wagner, W., and A. Pruß (2002), The IAPWS formulation 1995 for the thermodynamic properties of ordinary water substance for general and scientific use, *J. Phys. Chem. Ref. Data*, *43* (2), 387–535.
- Wibberley, C. A. J., and T. Shimamoto (2003), Internal structure and permeability of major-lip fault zones: the Median Tectonic Line in Mie Prefecture, southwest Japan, *J. Struct. Geol.*, *25*, 59–78.
- Wibberley, C. A. J., and T. Shimamoto (2005), Earthquake slip weakening and asperities explained by thermal pressurization, *Nature*, *436*(4), 689–692.
- Zhang, S., T. E. Tullis, and V. J. Scruggs (1999), Permeability anisotropy and pressure dependency of permeability in experimentally sheared gouge materials, *J. Struct. Geol.*, *21*, 795–806.
- Zheng, G., and J. R. Rice (1998), Conditions under which velocity-weakening friction allows a self-healing versus a cracklike more of rupture, *Bull. Seism. Soc. Am.*, *88*(6), 1466–1483.